Ph.D. DISSERTATION

Infrared Detection Using the Silicon Devices

(실리콘 기반 소자를 이용한 적외선 검출)

By

HuiJung Kim

August 2015

SCHOOL OF ELECTRICAL ENGINEERING AND COMPUTER SCIENCE
COLLEGE OF ENGINEERING
SEOUL NATIONAL UNIVERSITY

Infrared Detection Using the Silicon Devices

(실리콘 기반 소자를 이용한 적외선 검출)

指導敎授 朴 榮 俊

이 論文을 工學博士 學位論文으로 提出함
2015 年 **6** 月

서울大學校 大學院
電氣–컴퓨터 工學部
金 熙 中

金 熙 中의 工學博士 學位論文을 認准함
2015 年 **6** 月

委 員 長	박 병 국	(印)
副委員長	박 영 준	(印)
委 員	이 병 호	(印)
委 員	이 규 필	(印)
委 員	이 명 진	(印)

Infrared Detection Using the Silicon Devices

By

HuiJung Kim

Submitted to the School of Electrical Engineering and Computer Science
in partial fulfillment of the requirements for the degree of
Doctor of Philosophy in Electrical Engineering
at
SEOUL NATIONAL UNIVERSITY

August 2015

Committee in charge:

Byung Gook Park, Chairman
Young June Park, Vice-Chairman
Byoung Ho Lee
Kyu Pil Lee
Myung Jin Lee

Abstract

Lights in nature can be classified into various bands depending on the wavelength. Among the many types of light, near infrared (NIR) light has a wavelength of 780–2500 nm. The NIR wavelength band is widely used in various types of sensor devices, as well as in communication. Therefore, there is substantial demand for efficient and cost-effective NIR detectors. However, although materials such as InGaAs, Ge, and PbS are applied in detectors to detect NIR wavelengths, these materials are not compatible with the widely used and cost-effective Si-based integration process.

Thus, this dissertation focuses on detection of NIR light using a Si based device. However, the crucial obstacle in using Si as an NIR detection material is that it has band gap energy of 1.12 eV, and therefore, it does not absorb wavelengths longer than 1150nm. One possible solution is utilizing the Franz–Keldysh effect (FKE) in the Si devices. The FKE dictates that a semiconductor can absorb a photon with lower energy than the band-gap energy by tunneling the valence electrons to the conduction band in the presence of a strong electric field. This phenomenon can be used to detect infrared (IR) photons if the junction is biased in the FKE bias region.

In this dissertation, to investigate the detection of NIR with a Si-based device, we attempt to use the Zener diode and the NMOSFET, which can generate tunneling currents in the presence of a strong electric field. When a strong reverse bias is applied to the Zener junction, a tunneling current is generated; the NMOSFET also has a tunneling current when the bias condition generates a gate-induced drain leakage (GIDL) current. In such a bias condition for both devices, NIR with wavelengths of 1310nm and 1550nm, which have lower energy than the band-gap energy of Si, are irradiated to the Zener diode and the

NMOSFET. In the case of the Zener diode, an avalanche multiplication is investigated to cause more absorption by applying an additional, stronger electric field than the normal reverse bias condition, which causes a tunneling current to flow. However, because the negative temperature coefficient is due to the Joule heat generation of the junction in the bias regime of the avalanche multiplication, the methodology of a pulsed bias scheme is applied to mitigate the unintentional increase in the junction temperature and the associated degradation of the photo-responsivity under a DC bias. Accordingly, the NMOSFET in the condition in which GIDL flows can also absorb wavelengths of 1310nm and 1550nm by FKE. Additionally, the photo-generated current can be amplified by avalanche multiplication under a strong electric field with the pulsed bias scheme between the drain and the substrate.

Thus, this dissertation concludes that Si-based junctions can be used to detect IR signals using the FKE generation followed by multiplication through the newly proposed methodology of pulse measurement, which minimizes both the thermal effect and the degradation of photo-responsivity.

Keywords

Avalanche multiplication, Franz-Keldysh effect, Near Infrared, NMOS GIDL, Positive and negative temperature coefficient, Pulse measurement, Responsivity, Tunneling current, Zener diode

Student Number: 2011-30228

Contents

List of Tables

List of Figures

Chapter 1

Introduction

1.1 Motivation

Light rays in a nature are various, and are classified with distinctive energy depending on the wavelength. Among so many different light types, light that is defined in the particular range of 780–2500nm is called as near infrared (NIR) light. Specifically, 850nm, 1310nm, and 1550nm have conditions that are used for several types of sensors and communication in various fields [1]. These three types of NIR are selected depending on the communication distance: 850nm for short distances, 1310nm for middle distances, and 1550nm for long distances. In particular, the 1550nm wavelength is excellent for maximum optical fiber efficiency in the submarine fiber-optic cable used for intercontinental communications. In optical communication, the photodetector is an indispensable part of the receiver [1].

IR detectors are also widely used in real commercial products. The range of such applications is large, from simple devices that are used as remote controls for appliances such as televisions and air conditioners, up to high-performance products that are mounted on military weapons, satellite detectors, and sensors of various kinds. Typically, the wavelength of a certain region that a photodetector absorbs has larger energy than the band-gap energy of the detection material in

order to generate an electrical signal from the photodetector. Almost all photodetectors operate by this mechanism [2].

On the other hand, according to the energy of the light depending on the wavelength, the materials that can be used for the photodetector vary, and they are determined by the target wavelength to be detected. Materials such as Ge and InGaAs are used to detect infrared (IR) light in the 900–1700nm region [3]–[5], PbS is used for the 1700–2500nm region [2], and III-V materials such as InSb are used in the range of 2500–5000nm [2]. In the case of the 5000–9000nm region, II-V compounds such as HgCdTe are applied [6]. Due to the long wavelengths of IRs, these materials must have low band-gap energy relative to the normal transition mechanism of the photodetector [1]. Therefore, if the photodetector is operated at normal temperatures, high dark current by thermal generation inevitably flows [2]. Therefore, it is always necessary to reduce the temperature of the device with a cooler to reduce the high dark current [2]. In general, for these photodetectors, the electrical energy required for the normal operation below temperatures of 125 K is considerably large [6]. In addition, the materials for detecting light in these wavelengths require an expensive integration process. Attempts to integrate these low band-gap materials on Si substrates have encountered problems, such as the lattice mismatch with Si and the high defect density generation in the Si integration process [7]–[12].

Another competitive structure is the Schottky barrier detector (SBD), which is controlled by the metal silicide barrier to detect IR light [1], [65]–[67]. The Schottky barrier depends on the metal work function, which determines the IR wavelength that can be detected. In the case of nickel silicide, the Schottky barrier appears in the range 0.5–0.7eV (2.48–1.78μm), with a responsivity of 4.6mA/W, which is a low value [66]. This low responsivity is due to the

reflection on the metal silicide interface [66]–[67]. Although SBD can be a solution for Si-based IR detectors, the low responsivity issue is still a problem that must be solved [67].

Therefore, the purpose of this dissertation, to solve these problems, is to use conventional Si devices as photodetectors to detect NIR light. To detect NIR with Si-based devices, there are some obstacles to solve, such as the k-selection rule related with the indirect nature of the energy band gap in Si and greater band-gap energy than the energy of the IR wavelengths to be detected. This dissertation will present solutions for these problems, the significant results of the investigation, and future research directions for Si IR detectors.

1.2 Optical characteristics of Si for IR detectors

In general, light with a wavelength in a certain region that a photo detector absorbs has a higher energy than the band-gap energy of the detection material, thereby generating an electrical signal as previously mentioned. However, one of the most significant problems encountered when attempting to use Si as an IR detector is its extremely small absorption coefficient [13], [17]. The reason is that the band-gap energy of Si, 1.12eV, is larger than the energy of most IR wavelengths. When the IR energy is calculated from the wavelength, 1.12 eV corresponds to a wavelength of 1150nm. Thus, almost all IRs with a longer wavelength than 1150nm transmit without absorption in Si [13]. Table 1.1 shows the optical characteristics for IR wavelengths of 1310nm and 1550nm in detail. As shown in Table 1.1, the absorption coefficients for IR wavelengths of 1310 nm and 1550nm in Si are extremely small: 2.78×10^{-5}/cm and below 3.2×10^{-5}/cm, respectively [13]. Given these optical characteristics, Si appears to be

unusable as an IR detector [13]–[17]. However, when a special bias scheme is applied to the Si devices, the Franz–Keldysh effect (FKE) makes it possible to increase the absorption coefficient of the IR wavelengths that have lower energy than the Si band-gap energy.

	Refractive index(n)	Absorption Coefficient	Refractive index(n)	Absorption Coefficient
Wavelength	1310nm		1550nm	
Glass	1.5099	0.50952 /cm	1.5070	0.32060 /cm
Si (300K)	3.503	2.7×10^{-5} /cm	<3.486 (1450nm)	$<3.2\times10^{-8}$ / cm (1450nm)
SiO_2	1.4468	-	1.4440	-
Si_3N_4	<1.9827	-	<1.9827	-

Table 1.1 Optical characteristics of Si with infrareds of 1310nm and 1550nm

1.3 Common view of the Franz-Keldysh effect

In general, to absorb IR photons in Si, the energy of the IR light must be larger than the band-gap energy of Si in order to generate an electrical signal, as previously mentioned. Because the IR energy is smaller than the Si band-gap energy, it may be impossible to absorb IR in the semiconductor. However, one of the possible solutions is utilizing the FKE in the semiconductor devices [18].

Under the FKE, the semiconductor can absorb photons with a lower energy than the band-gap energy, by tunneling the valence electrons to the conduction band in the presence of a strong electric field [18]–[20]. The phenomenon may be used to detect IR photons if the junctions are biased in the FKE bias region. The FKE will be discussed in more detail in Chapter 2.

1.4 Si devices for an IR photo detector

It is observed that IR wavelengths above 1150nm have lower energy than the Si bandgap energy as explained previously. Hence, it may be impossible to absorb these wavelengths in Si. One of the possible solutions is utilizing the FKE [18]–[25] in the silicon devices. The phenomenon may be used to detect IR photons if the junctions are biased in the FKE bias region. This phenomenon is analogous to trap-assisted tunneling, except that the trap states are not mandatory in the case of FKE tunneling. Even though several attempts [25]–[28] have been made to realize an IR detector using the silicon, such as nanowire PN junctions [26], the behavior of conventional silicon junctions, such as the Zener diode junction in the strong reverse bias region [29]–[35] and the MOSFET in the gate induced the drain leakage (GIDL) bias condition [36]–[55], have not been reported. In addition, the Zener diode in the strong reverse

bias region is governed by the tunneling current followed by the avalanche multiplication [30]–[32], which may be used to amplify the IR signal generated by the FKE. Further, the GIDL tunneling current can be multiplied by the avalanche mechanism when the strong bias between the drain and the substrate is applied to increase lateral electric field at the surface junction [38]–[40], [52]–[54]. The lateral electric field is analogous to the surface electric field in the sense that each direction of the electric field is different from each other at the surface junction. For experimental devices, the Zener diode and the NMOSFET, which are Si-based devices, are investigated as optical detectors for IR wavelengths.

1.5 Infrareds laser sources

For the light sources in the experiments, IR wavelengths of 808nm, 1310nm, and 1550nm were chosen. In particular, 850nm, 1310nm, and 1550nm have important roles in that they are used for communication in various fields as explained in Section 1.1. In particular, the 1550nm IR has maximum optical fiber efficiency in fiber-optic cable used in communications among continents [1]–[2]. For the IR sources, lasers were used with wavelengths of 808nm, 1310nm, and 1550nm, and optical output powers of 5 mW, 5 mW, and 10 mW, respectively, in the operating bias condition, as listed in Table 1.2. The lasers are illuminated in normal incidence from the top of the Zener diode and the NMOSFET.

Wavelength	Operating Current	Light Energy	Optical output Power
808nm	50mA	1.56eV	5mW
1310nm	30mA	0.95eV	5mW
1550nm	50mA	0.80eV	10mW

Table 1.2 Infrareds laser sources with the wavelength of 808nm, 1310nm and 1550nm

1.6 Outline of the Dissertation

The primary purpose of this dissertation is to understand the technical challenge associated with using the FKE effect to detect IR photons with the conventional silicon tunneling junctions; the Zener diode and the MOSFET as experimental devices.

Chapter 2 briefly reviews the existing Franz-Keldysh effect which dictates that the semiconductor can absorb a photon with lower energy than the band-gap energy by tunneling of the valence electrons to the conduction band in the presence of high electric field. Tunneling current mechanism and phonon assisted tunneling are discussed on theoretical framework.

In chapter 3, the response of the devices for the IR photons under various bias conditions with the Zener diode is discussed. Unintentional increase in the junction temperature and the associated degradation of the photo-responsivity under the DC bias are discussed. As well, a pulsed bias scheme is introduced to mitigate the thermal effect that degrades the photo sensitivity. Experimental data for the Zener junction which is commercially available is demonstrated and discussed.

In chapter 4, the response of the devices to the IR photons under various bias conditions with the surface junction (the source and the drain) of a NMOSFET (fabricated in house) is investigated. At first, the structure of NMOSFET which is designed by our group is explained as an experimental device for infrareds photo detector. Experimental data and the surface junction of a NMOSFET are demonstrated and discussed.

In chapter 5, it is presented about the effects of the avalanche multiplication of FKE generated current in the MOSFET device under infrareds. In order to see the

potential of the impact ionization following the FKE generation in the case of NMOSFET, the experiment which applies various bias schemes to the substrate is performed under infrareds. In addition, simulated results are discussed including modeled structure, band to band tunneling profile, and electric field profile at the surface junction. The result of calculated absorption coefficient from simulated electric field profile is also discussed with the experimental results in this chapter.

Finally, the conclusion of the present work is given together with the summary for further study in chapter 6.

Chapter 2

Fundamentals of optical transition in Silicon

2.1 The Franz-Keldysh effect

Generally, larger energy of the infrared than the band gap energy of Si has to be irradiated to generate an electrical signal and to absorb photons. Because the energy of near infrareds over 1150nm is smaller than Si bandgap energy, it may be impossible to absorb in Si. However, one of possible solutions is utilizing the Franz-Keldysh effect (FKE) in the silicon devices [18]. Under the FKE, the semiconductor can absorb photons of lower energy than the band-gap energy by tunneling of the valence electrons to the conduction band in the presence of high electric field as shown in Fig. 2.1 [18]-[20]. The phenomenon may be used to detect the IR photon if the junctions are biased in the FKE bias region.

Let us consider the case of a uniform applied electric field, V(r) = e**F**·**r**. The Schrődinger equation for the wave function φ(**r**) is

$$\left[-\frac{\hbar^2}{2m^*}\nabla^2 + e\mathrm{F}\bullet\mathrm{r}\right]\phi(r) = E\phi(\mathrm{r}) \qquad (2.1.1)$$

$$\mathrm{F} = \hat{\mathrm{z}}F \quad , \quad \phi(\mathrm{r}) = \frac{e^{ik_x x + k_y y}}{\sqrt{A}}\phi(z) \qquad (2.1.2)$$

$$\left[-\frac{\hbar^2}{2m^*}\frac{d^2}{dz^2}+eFz\right]\phi(z)=E_z\phi(z) \tag{2.1.3}$$

$$E=\frac{\hbar^2}{2m^*}(k_x^2+k_y^2)+E_z \tag{2.1.4}$$

The solution of the Schrődinger equation (2.1.3) under uniform field can be obtained.

$$Z=\left(\frac{2m^*eF}{\hbar^2}\right)^{1/3}\left(z-\frac{E_z}{eF}\right) \tag{2.1.5}$$

$$\frac{d^2\phi(z)}{dz^2}-Z\phi(z)=0 \tag{2.1.6}$$

The solutions for the equation is the Airy function Ai (Z). Because the wave function has to decay as z approaches $+\infty$, the Airy function Ai (Z) has to be chosen. The energy spectrum is continuous because the potential is not bounded as z $\rightarrow$ $-\infty$. Therefore, the wave function satisfying the normalization condition

$$\int_{-\infty}^{\infty}dz\phi_{E_{z1}}(z)\phi_{E_{z2}}(z)=\delta(E_{z1}-E_{z2}) \tag{2.1.7}$$

$$\phi_{E_z}(z)=\left(\frac{2m^*}{\hbar^2}\right)^{1/3}\frac{1}{(eF)^{1/6}}Ai\left[\left(\frac{2m^*eF}{\hbar^2}\right)^{1/3}\left(z-\frac{E_z}{eF}\right)\right] \tag{2.1.8}$$

The sum over all the states n for the absorption spectrum has to be replaced by the sum over all the quantum numbers

$$\sum_n\rightarrow\sum_{kx}\sum_{ky}\int dE_z \tag{2.1.9}$$

Where the sum over the energy Ez is an integral because Ez is a continuous spectrum and a delta function normalized has been adopted.

Therefore,

$$\alpha(\hbar\omega) = A_0^2 \sum_{kxky} \int dEz \left|\phi(\mathrm{r}) = 0\right|^2 \delta\left[\frac{\hbar^2}{2m^*}(k_x^2 + k_y^2) + E_z + E_g - \hbar\omega\right] \tag{2.1.10}$$

$$\frac{2}{A}\sum_{kxky} = 2\int \frac{d^2k_t}{(2\pi)^2} = \frac{m^*}{\pi\hbar^2}\int dE_t \tag{2.1.11}$$

Where $E_t = \frac{\hbar^2}{2m^*}(k_x^2 + k_y^2) = \frac{\hbar^2 k_t^2}{2m^*}$, the integral is carried out over Et with the delta function and obtain for the absorption coefficient as follows

$$\alpha(\hbar\omega) = A_0 \frac{m^*}{\pi\hbar^2} \int_{-\infty}^{\hbar\omega - E_g} dE_z \left(\frac{2m^*}{\hbar^2}\right)^{2/3} \frac{1}{(eF)^{1/3}} Ai^2\left[\left(\frac{2m^*}{\hbar^2 e^2 F^2}\right)^{1/3}(-E_z)\right] \tag{2.1.12}$$

$$\alpha(\hbar\omega) = \frac{A_0}{2\pi}\left(\frac{2m^*}{\hbar^2}\right)^{3/2} \sqrt{\hbar\theta_F} \int_{\eta}^{\infty} d\tau E_z Ai^2(\tau)$$

$$= \frac{A_0}{2\pi}\left(\frac{2m^*}{\hbar^2}\right)^{3/2} \sqrt{\hbar\theta_F}\left[-\eta Ai^2(\eta) + Ai'^2(\eta)\right] \tag{2.1.12}$$

where, $\hbar\theta_F = \left(\frac{\hbar^2 e^2 F^2}{2m^*}\right)^{1/3}$ $\tau = -E_z/(\hbar\theta_F)$, $\eta = \left(E_g - \hbar\,\omega\right)/\hbar\theta_F$. (2.1.13)

As shown in the equation of absorption coefficient, the equation depends on electric field significantly [21]-[26], [56]. This phenomenon is analogous to the trap assisted tunneling, except that the trap states are not mandatory in the case of the FKE tunneling.

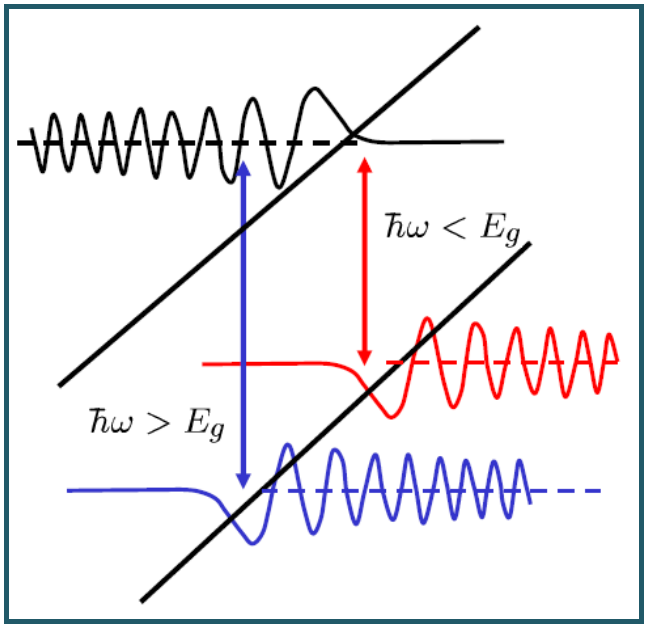

Fig. 2.1 A Schematic band diagram with the state of wave function under strong electric field [20]

2.2 Tunneling current based on the Franz-Keldysh effect

2.2.1 Tunneling Probability

When the electric field is sufficiently high, a probability exists for inter-band tunneling, that is direct transition of electrons from the valence band to the conduction band. The tunneling probability T can be given by the WKB (Wentzel-Kramers-Brillouin) approximation [46].

$$T \approx \exp\left[-2\int_{0}^{x_2} |k(x)|\, dx\right] \tag{2.2.1}$$

Where $|k(x)|$ is the absolute value of the wave vector of the carrier inside the barrier, and x=0 and x_2 are the classical boundaries (both edge of depletion region at the junction).

The tunneling of an electron through a forbidden band is formally the same as a particle tunneling through a potential barrier.

$$k(x) = \sqrt{\frac{2m^*}{\hbar^2}(PE - E_c)} \tag{2.2.2}$$

where PE is the potential energy. For tunneling, the incoming electron has a PE equal to the bottom of the energy gap. The value inside the square root is thus negative and k is imaginary. Furthermore, the various conduction band edge E_c can be expressed in terms of the electric field F. The wave vector inside the triangular barrier is given by

$$k(x) = \sqrt{\frac{2m^*}{\hbar^2}(-qFx)} \tag{2.2.3}$$

$$T \approx \exp\left[-2\int_{0}^{x_2} \sqrt{\frac{2m^*}{\hbar^2}(qFx)}\, dx\right] \tag{2.2.4}$$

For a triangular barrier with a uniform field, $x_2 = E_g / Fq$, the result is

$$T \approx \exp\left(-\frac{4\sqrt{2m^*}E_g^{3/2}}{3q\hbar F} \right) \tag{2.2.5}$$

From the tunneling probability, the tunneling current is calculated [46].

2.2.2 Tunneling current of the Zener diode

When the strong reverse bias is applied to the high doped PN diode, the width of depletion region is

$$W = \left(x_p + x_n \right) = \sqrt{\frac{2\varepsilon}{q}\left(\frac{1}{N_A} + \frac{1}{N_D} \right)\left(V_{bi} + V_R \right)} \tag{2.2.6}$$

Tunneling current density for the Zener diode is shown at (2.2.7) under reverse bias of V_R with maximum electric field of (2.2.8) [42].

$$J_{BTB} = qN_V T\nu = qN_T \nu = \frac{\sqrt{2m^*}V_R F}{4\pi^3\hbar^2\sqrt{E_g}} \exp\left(-\frac{4\sqrt{2m^*}E_g^{3/2}}{3q\hbar F} \right) \tag{2.2.7}$$

$$F_{\max} = \sqrt{\frac{2qN_A N_D (V_{bi} + V_R)}{\varepsilon_{si}(N_A + N_D)}} \tag{2.2.8}$$

2.2.3 Gate Induced Drain Leakage current of NMOS

When strong bias is applied at the junction between the drain and the gate, there can be tunneling current which is called Gate Induced Drain Leakage current (GIDL) [51]-[52], [68].

Depletion width is

$$W = \sqrt{\frac{2\varepsilon_{si}\psi_s}{qN_0}} \tag{2.2.9}$$

Vertical electric field is . $E_{si} = \sqrt{\frac{2\psi_s q N_0}{\varepsilon_{si}}}$ (2.2.10)

In addition, from Gaussian law,

$$\varepsilon_{si} E_{si} = \varepsilon_{ox} E_{ox} = \varepsilon_{ox} \frac{V_{dg} - V_{fb} - \psi_s}{T_{ox}} \quad (2.2.11)$$

Where,

E_{ox} electric field across SiO2, T_{ox} oxide thickness,

V_{fb} flatband voltage,

ε_{ox} dielectric constant of the oxide.

Surface potential is

$$\psi_s = V_{dg} - V_{fb} + \frac{q N_0 T_{ox}^2 \varepsilon_{si}}{\varepsilon_{ox}^2} - \sqrt{\left(\frac{V_{dg} - V_{fb} + q N_0 T_{ox}^2 \varepsilon_{si}}{\varepsilon_{ox}^2} \right)^2 - (V_{dg} - V_{fb})^2} \quad (2.2.11)$$

, where V_{dg} is the voltage of junction between the gate and the drain.

Tunneling current is shown as

$$I_{GIDL} = A E_{si} \exp\left(-\frac{B}{E_{si}} \right) \quad (2.2.12)$$

Where $A = \frac{q^3 m_e}{2\pi^2 \hbar^3}$, $B = \frac{\pi m_e^{1/2} E_g^{3/2}}{2\sqrt{2} q \hbar}$ [68].

2.3 Phonon-assisted tunneling in the indirect band gap of semiconductor

Silicon must have the help of phonon energy for electrons to tunnel into the conduction band from the valence band due to the indirect material of Si. Indirect band gap of silicon as an electronic material has the meaning of the optical transition to be constructed in E-k diagram as followed; delta k momentum must be conserved to go into minimum point of the conduction band from the maximum point of valence band [41]-[42]. This means that not only photons but the interaction of phonon is also demanded to occur for the transition of electrons. The former is obtained in the transition energy from the photon. However, maximum phonon energy of 66meV is very small compared to the bandgap energy of silicon [41]. When electrons make a transition optically, most of the energy is gained by photons. Further, in this transition, the wave vector k must be also supplied as well. Wave vector of photon E_{photon} / ħc, where E_{photon} of 1eV, is a value of about 2×10^5 [m^{-1}] which is very small compared to k_c ($=0.8\times 2\pi/a$, wave vector at the minima of conduction band) [41]. On the other hand, $k_{phonon} = \pi/a$ which is the case of Si in the Brillouin zone edge vicinity, is comparable to the wave vector of the electron k_c [41].

2.4 Photo responsivity

Generally, when photo current is generated by injected photon flux to the devices, photon flux $\Phi(\lambda)$ (=the number of incident photons per second per unit area) of monochromatic radiation at a wavelength λ is defined [56].

$$\Phi(\lambda) = \frac{P_\lambda}{h\nu A} \tag{2.4.1}$$

Where A is the photodetector illumination area, and P_λ is the input optical power at a wavelength, we can write the photo current

$$i = q\eta\Phi(\lambda)A = q\eta\frac{P_\lambda}{h\nu} \tag{2.4.2}$$

, and η is the quantum efficiency of the photodiode including the effects of the intrinsic quantum efficiency, the reflection, and absorption depth. The photo current responsivity is shown as

$$R = \frac{i}{P} = \eta\frac{q}{h\nu} \tag{2.4.3}$$

Chapter 3

IR detection with the Zener diode

3.1 Zener diode as a photodetector

In this chapter, the Zener diode that is typical Si based device and commercially available, is investigated to detect near infrareds for technical challenge as infrareds detector.

3.1.1 Reverse Current characteristics of the Zener junction

To investigate the possibility of detecting IR by FKE, one of devices which are governed by tunneling mechanism has been chosen such as the Zener diode. As shown in Fig. 3.1, the scheme of PN junction in the Zener diode which has a depletion region is shown when the strong reverse bias is applied at the PN junction. In the depletion region under strong uniform electric field, there can be the steep slope of the conduction band and the valence band. Due to strong electric field, tunneled states at reverse biased PN junction can exist within forbidden band gap. Because delta energy between tunneled states of both band edges becomes lower than silicon bandgap energy, photo current can be generated by lower energy of near infrareds than Si bandgap energy. And the

photo generated current which means FKE by near infrareds is multiplied in avalanche breakdown regime additionally in the case of the PN junction.

Fig. 3.2 shows that electrons in the valence band may tunnel to the conduction band if the IR photon energy transfers for electrons of the valence band from A point in the forbidden gap followed by tunneling to B state in the conduction band state. The tunneling distance from A to B is $W = (E_g - \hbar\omega)/qF$, where E_g and $\hbar\omega$ are the bandgap energy and IR photon energy, respectively, and F is the electric field intensity, which is assumed to be constant between A and B in the Fig. 3.2 . As the tunneling current is dependent on W in an exponential manner [46], photons of $\hbar\omega$ ($< E_g$) may be detected if F is large enough. The photo generated electron and hole pairs may be multiplied by the avalanche multiplication [38]-[44] if the carrier path to the contacts is identical for electrons and holes. For the Zener diode in Fig. 3.2, both carriers are heated up by the same electric field. Specially, to show the IR detection with affordable device to get, the commercial Zener diode has been investigated in this experiment.

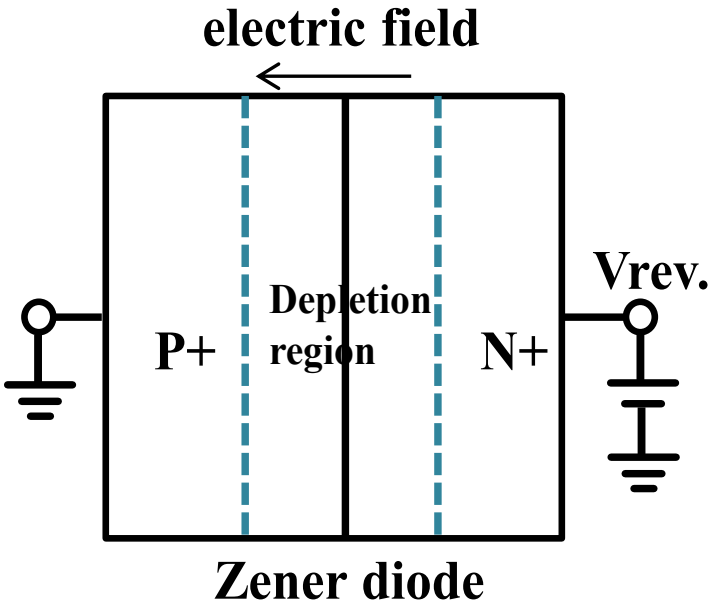

Fig. 3.1 Schematics of the Zener junction

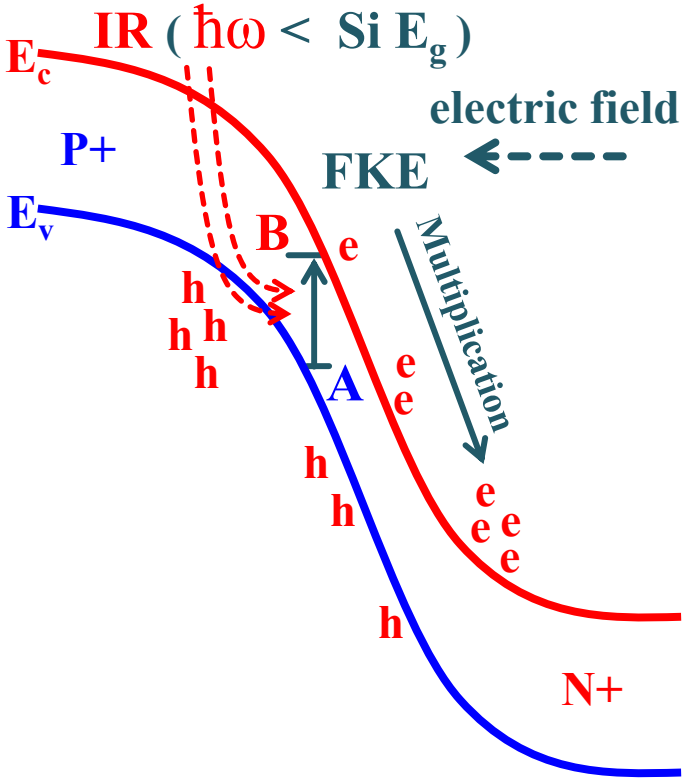

Fig. 3.2 Energy band diagrams in the FKE bias conditions for the Zener junction

3.1.2 Feature of the experimental Zener diode

As an experimental device, the device has to be chosen under the satisfaction of two constraints; first constraint is what the device has been fabricated with Si material for the junction. Second constraint has the mechanism what the current is governed by tunneling under strong electric field to generate photo current by Franz-Keldy effect. One of the possible devices that give the satisfaction of two constraints is the Zener diode under strong reverse bias. For the Zener diode, commercial device has been used with the model of TC1N4737A made by TAK CHEONG Co. which has zener breakdown voltage of 7.5V as shown in Fig. 3.3. The device has the sealed package of DO-41(JEDEC) through which the infrareds can be illuminated at the junction. Through packaged glass, infrareds can be illuminated into the PN junction that is located between two electrodes.

Fig. 3.3 Image of conventional Zener diode which has the breakdown voltage of 7.5V

3.1.3 Temperature coefficient of the reverse current

In this section, let's look at the temperature coefficient which is related to the current mechanism briefly.

For the tunneling current and the bandgap as denoted at (3.1.3.1) and (3.1.3.2) respectively, there is the positive temperature dependency which is related to the band gap reduction as the temperature increases [38].

$$J_t = \frac{\sqrt{2m^*}q^3 E_p V_a}{4\pi^3 \hbar^2 E_g^{1/2}} \exp\left(\frac{-4\sqrt{2m^*}E_g^{3/2}}{3qE_p\hbar}\right) \tag{3.1.3.1}$$

$$E_G(T) = E_G(0) - \frac{\alpha T^2}{T+\beta} \tag{3.1.3.2}$$

However, avalanche breakdown voltage has the negative temperature coefficient. As shown below equation, breakdown voltage increases as the temperature is increased. It is resulted that the current is reduced as the temperature is increased [33], [40].

$$V_B(T) = V_B(T_o)\,[1 + \beta(T\text{-}T_0)] \tag{3.1.3.3}$$

where T_0 is room temperature, $\beta = 8.8\times10^{-4}/℃$.

Mean free path for an impact ionization decreases due to phonon scattering which is caused by junction heating. Therefore, the energy which is necessary to be impact ionized decreases from the phonon scattering. Thus, stronger bias is needed to be the same current at the higher temperature than at room temperature.

3.2 DC Measurement

3.2.1 Degradation in photo sensitivity

At first, the photo response has been measured under near infrareds. Figs. 3.4 and 3.5 shows the I-V data and the net photo current of the Zener diode in the DC bias mode, under the radiation of 808, 1310 and 1550nm. The net photocurrent is obtained by subtracting the dark current from the total current. There are three definitive regions denoted as Region I, II and III in Fig. 3.4 according to the sensitivity. The sensitivity in Region I (low bias) under the illumination 1310nm and 1550nm is caused by the Shockley Read Hall type generation through the traps. The net photo current in Fig. 3.5 shows that the current generated under the 1300nm and 1550nm lasers increases as the bias voltage increases in the tunneling region followed by drops in the higher bias region, which may be the negative effect resulted from the self-generated Joule heating. Thus, the decrease in the photo-sensitivity at the high bias region in Fig. 3.5 may be speculated to be caused by the negative temperature coefficient of the avalanche multiplication. The photo generated current resulted from the FKE is further multiplied by the avalanche effect in the high bias region. However, the self-generated heat may cause degradation in the multiplication, thereby reducing the photo sensitivity.

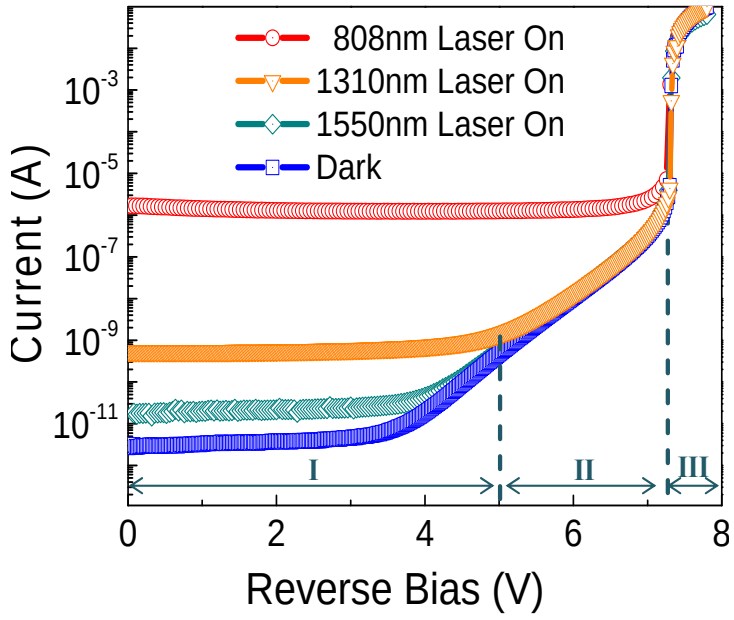

Fig. 3.4 I-V plot under various conditions; the dark, 808nm, 1310nm and 1550nm of infrareds

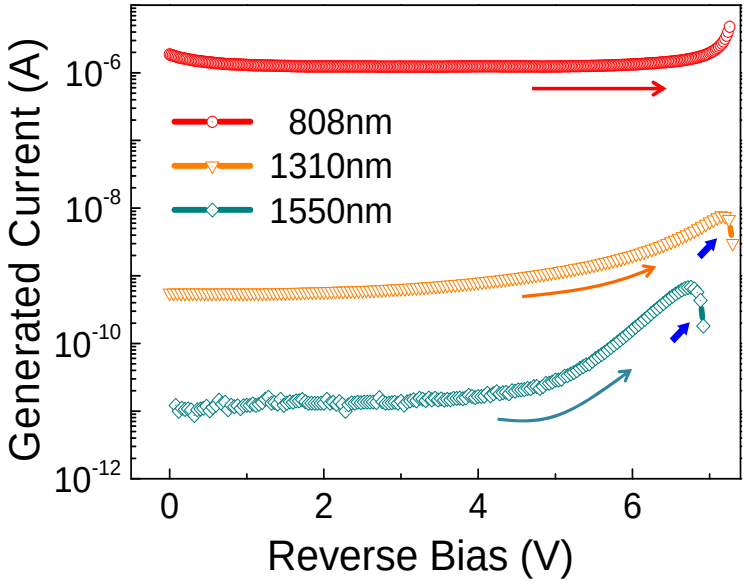

Fig. 3.5 Photo generated current vs. DC reverse bias under various light sources; 808nm, 1310nm, and 1550nm of infrareds

3.2.2 Temperature dependency of the photo sensitivity

In order to clarify the temperature effect by Joule heating at the junction, the dark current has been measured under various temperatures as shown in Fig. 3.6. In this figure, three distinctive bias regions are observed in terms of the relation between the dark current and the temperature; positive correlation in the Region I dominated by the SRH generation in the low bias region, negative correlation in the Region III dominated by the avalanche multiplication and both the positive and negative correlations in Region II where the tunneling and the avalanche cancel each other [38]. Also, the measurement is performed to investigate the junction heating by continuous several measurements under dark. As shown in Fig. 3.7, dark current is plotted by applying reversed bias with 5 times of the measurement continuously. As the times of a measurement increase, the breakdown voltage decreases in the avalanche multiplication bias region (III) which means negative temperature coefficient by Joule heating at the junction.

In the following section, the pulsed bias scheme is applied to reduce the negative temperature coefficient of the avalanche multiplication caused by the self-heating effect. As the temperature is increased at the junction, breakdown voltage is

$V_B(T)=V_B(T_o)[1+\beta(T-T_0)]$, where T_0 is room temperature, $\beta = 8.8\times10^{-4}/℃$ [33], [40].

As shown in above equation, breakdown voltage is decreased as the temperature is increased. Thus, we can conclude that the current is decreased as the temperature is increased at the avalanche breakdown regime.

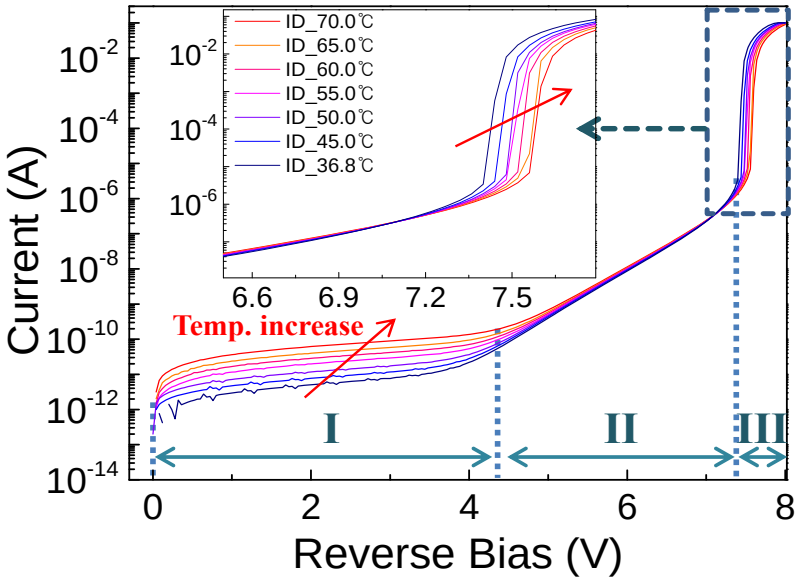

Fig. 3.6 I-V plot in the dark for various temperature conditions, three distinctive bias regions can be observed. The inset is the magnified plot in Region III (the avalanche multiplication region).

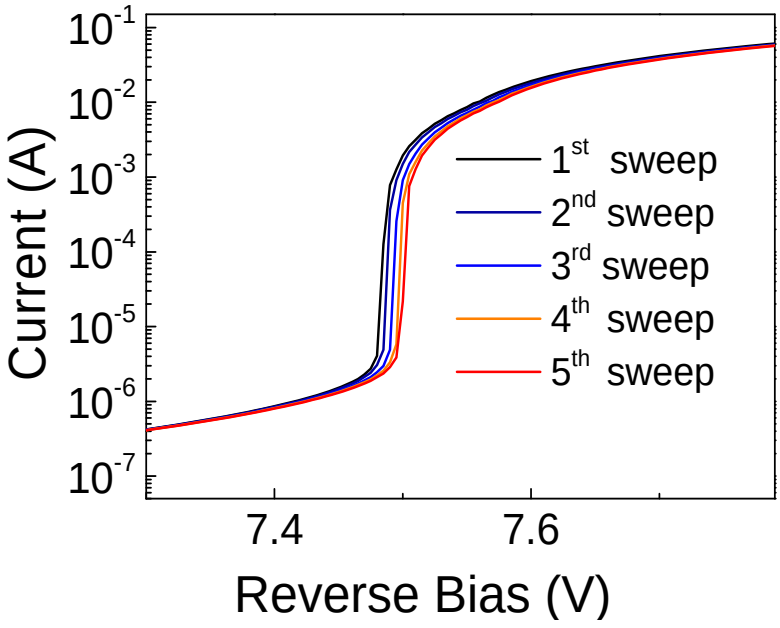

Fig. 3.7 Current vs. DC reverse bias under the dark condition is plotted with 5 times of measurement continuously.

3.3 The pulsed bias scheme

3.3.1 Circuit diagram for pulsed bias scheme

In previous section, the photo sensitivity is degraded by the self-generated heat in the bias regime of a multiplication. This negative temperature effect bothers to increase the photo responsivity of infrareds by Franz-Keldysh effect.

In order to mitigate the temperature effect as mentioned, pulsed bias was applied to the Zener diode where the pulse train bias was patterned with the width of 50μs (in every 500 μs.). In this experiment, the laser source has been biased with the pulse synchronized with the sensor even though the IR signal does not have to be synchronized with the photo-receiver in the real applications. Vin+ of OP amplifier is grounded in the circuit for the Zener diode of Fig. 3.8. Additionally, the pulse width of 50μs is chosen to be long enough for the junction to reach the steady state needed to maintain the FKE and the avalanche multiplication. Fig. 3.11 shows the photo-generated current according to the different pulse peak voltage. Indeed, the decrease in the sensitivity observed in Fig. 3.5 disappears for both the 1310nm and 1550nm indicating that the unwanted thermal effect was removed by the pulsed bias scheme. In the next section, the experimental data from both the Zener diode and MOSFET are described in detail.

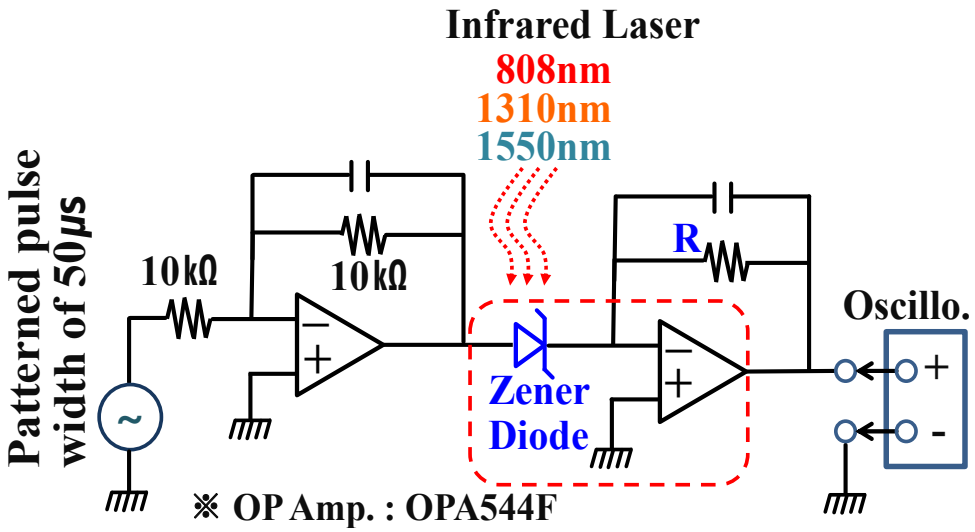

Fig. 3.8 Circuit which generates pulses to operate the Zener diode with the illumination of infrareds (808nm, 1310nm, and 1550nm), patterned pulse train with a 50 μs peak in every 500 μs is applied to the Zener diode.

3.3.2 Response of the input pulsed wave

Using the circuit as introduced in previous section, generated pulse train is shown at Fig. 3.9 (a). Patterned input pulse operates the Zener diode and lasers. A 10 kHz pulse with a 50% duty cycle is applied for the lasers (only experimental purpose) and a patterned pulse train is used for the Zener diode.

After operating the Zener diode, output voltage is measured by the oscilloscope. Fig. 3.9 (b) shows the example of delta output voltage by the Zener diode resulting from the laser of 1550nm on/off at the pulse input peak bias of 7.8V. Each output pulse is subtracted to extract the delta voltage which is generated by the infrared laser. In this way, the output voltage measurement is performed at amplitudes from 0V to 7.8V (steps 0.01V or 0.05V).

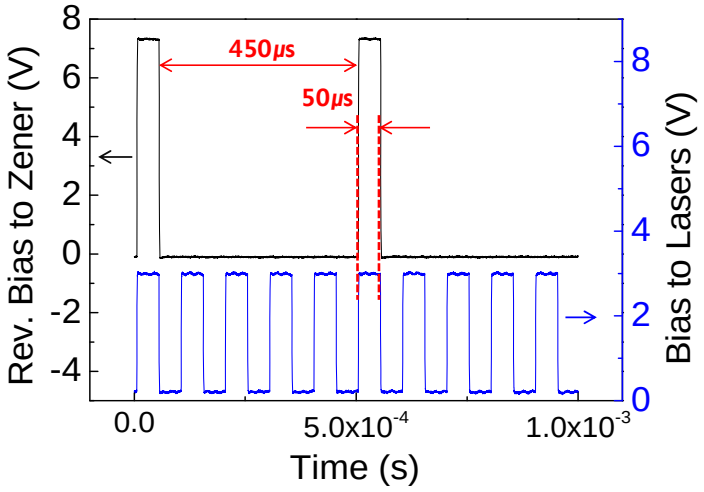

(a)

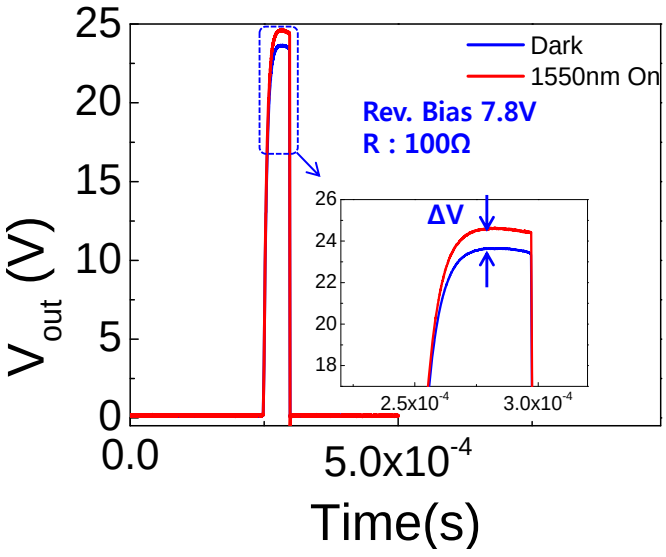

(b)

Fig. 3.9 (a) Patterned pulses applied to the Zener diode and the infrared laser. (b) 1550nm on/off switching at the pulse amplitude of 7.80V. Each output pulse is subtracted to extract the delta voltage caused by the infrared laser.

3.4 IR Photo response in the pulsed bias scheme

3.4.1 Bias dependency of photo generated current

Using the circuit and the pulse bias scheme described in the previous section, pulsed reverse peak voltage is applied to the Zener diode. In accordance with the infrared laser on/off, delta output voltage is generated from the optical response. Pulsed input voltage with infrareds on/off for the reverse bias of 1V, 5V, and 6.9V is shown at the Fig. 3.10, respectively. Accordingly, delta output voltages are shown for each reverse pulsed peak bias. The arrows mean that the photo generated response increases as the reverse bias increase showing the bias dependency above reverse bias of 5V.

From the delta voltage between the dark and the infrared on condition, photo generated current under the irradiation of three lasers (808nm, 1310nm and 1550nm) is measured using the Zener diode. The plot of photocurrent vs. the magnitude of the pulsed bias voltage in Fig. 3.11 now exhibits three regions: Region I, which is flat and determined by the SRH generation; Region II, which shows an increase in the photo-response due to the FKE and Region III, where the current photo-generated by the FKE is further amplified by the avalanche multiplication for both the 1310nm and 1550nm lasers. As compared with the DC measurement at Fig. 3.5, the pulsed bias condition gives the photo generated current consistently increase with the bias in the region II (FKE region) for both under the 1310nm and 1550nm lasers without the degradation. For the case of 808nm laser, the photo current shows negligible bias dependency even in tunneling current bias of Region II due to larger energy of 808nm IR than the silicon bandgap energy.

Furthermore, in the Region III, the photo generated current by the FKE shows

significantly steeper increase with the bias compared with the Region II, which indicates that the photo current by FKE is multiplied by an avalanche mechanism without the negative effect caused by the self-heating effect.

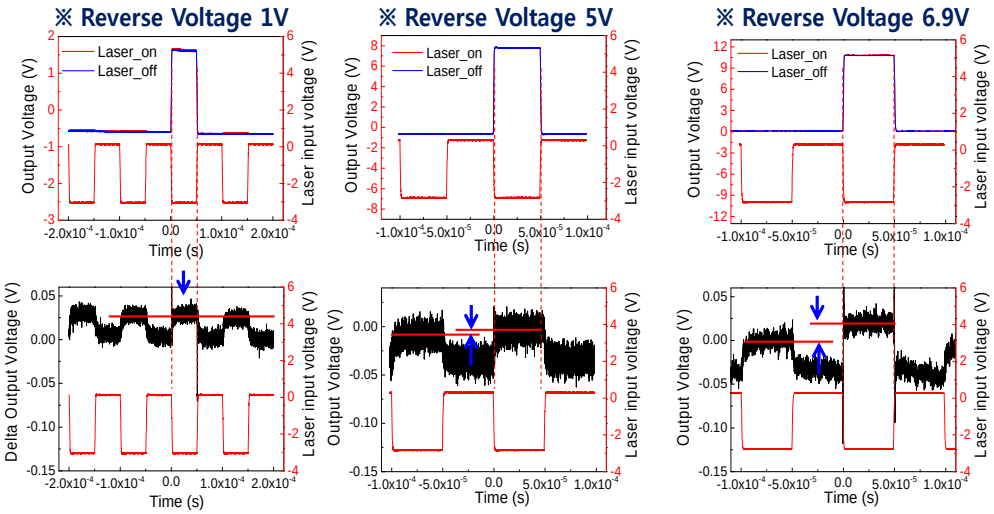

Fig. 3.10 Pulsed input voltage under infrared on/off conditions for the reverse bias of 1V, 5V, and 6.9V, respectively. Delta output voltage is shown for each reverse pulsed peak bias. The blue arrows mean that the photo generated response increases as the reverse bias increase showing the bias dependency above reverse bias of 5V.

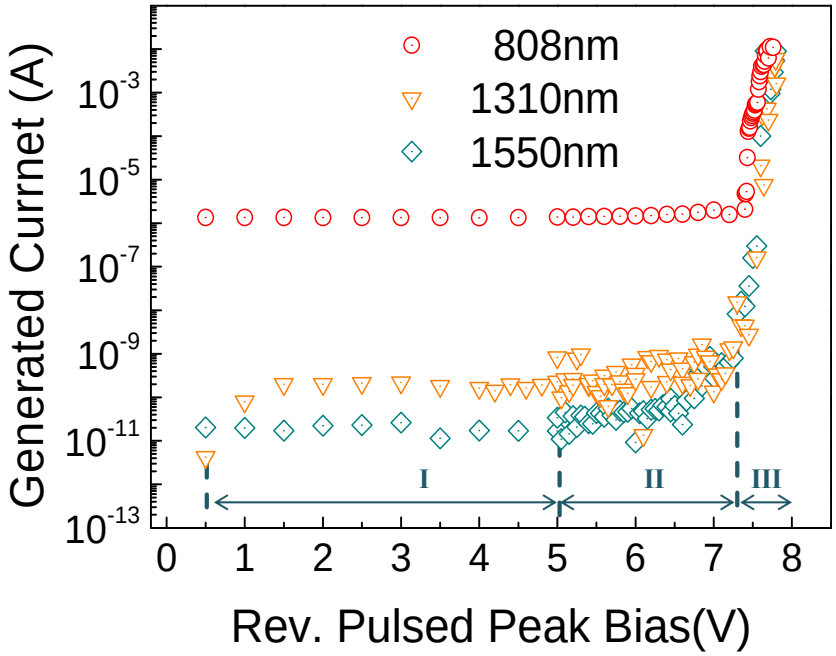

Fig. 3.11 Photo-generated current vs. pulsed voltage magnitude for the 808nm, 1310nm and 1550nm of infrareds

3.4.2 Photo responsivity for the infrared signal

The responsivities for 808, 1310 and 1550nm wavelengths are shown in Fig. 3.12 with the change in the pulse peak voltage. When the electric field is low, the responsivity for the 808nm laser is much higher than that for the 1310nm and 1550nm lasers. However, as the electric field increases, the responsivity for the near infrared lasers of 1310nm and 1550nm approaches that of the 808nm case (as much as 1.18A/W and 0.89 A/W for the 1310 and 1550nm, respectively). This means that the silicon based Zener diode may be used to detect near infrared light at wavelengths even larger than 1550nm as a result of the avalanche multiplication of the FKE generated photo current under the pulsed bias condition.

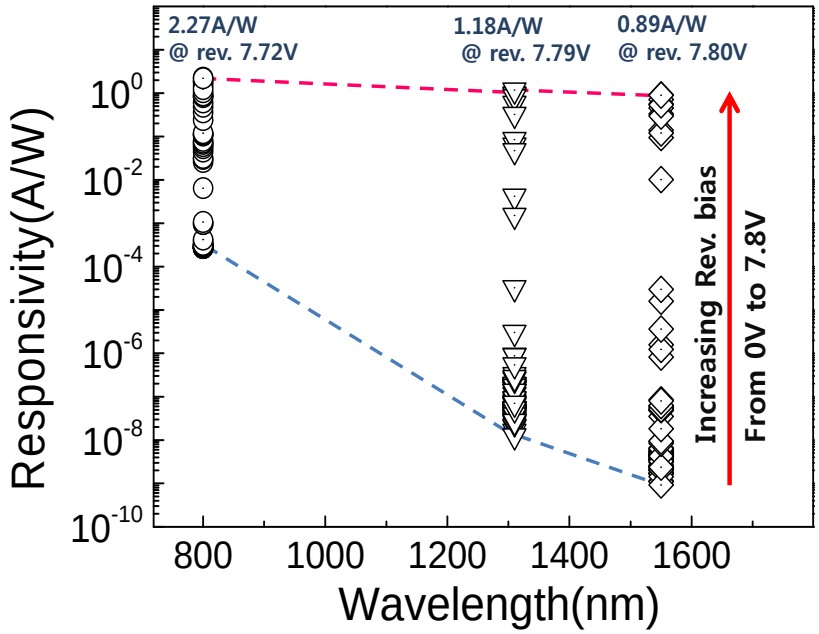

Fig. 3.12 Responsivity vs. wavelength (808nm, 1310nm and 1550nm), data for different pulsed bias voltages are shown.

3.5 Effect of defects in the junction on the FKE

3.5.1 Correlation of the FKE current with the trap density

In this section, we will discuss the effects of the defects in the junction on the FKE. As mentioned in section II, the FKE is similar to the TAT (trap assisted tunneling) in the sense that the trap residing in the band gap in the tunneling junction provides the step stone for the valence electrons before tunneling to the conduction band. In the FKE, the step stone is provided by the IR photon energy. In order to check the effects of the trap on the FKE effect in the Zener diode, we plot the correlation between the trap density and the FKE current using 20 different Zener diode samples. As the indicator of the trap density, we use the thermal leakage current in the low reverse bias condition under the dark (at reverse V=2.0V, for example) condition, which is believed to be dominated by the SRH generation. Fig. 3.13 shows that there is no correlation between the trap density and the FKE current at the same electric field of bias (measured in Region II) for each Zener diode, meaning that the increase in the tunneling current is dominated by the FKE effect .The observation is positive to the usage of the Zener type diode as the IR sensor.

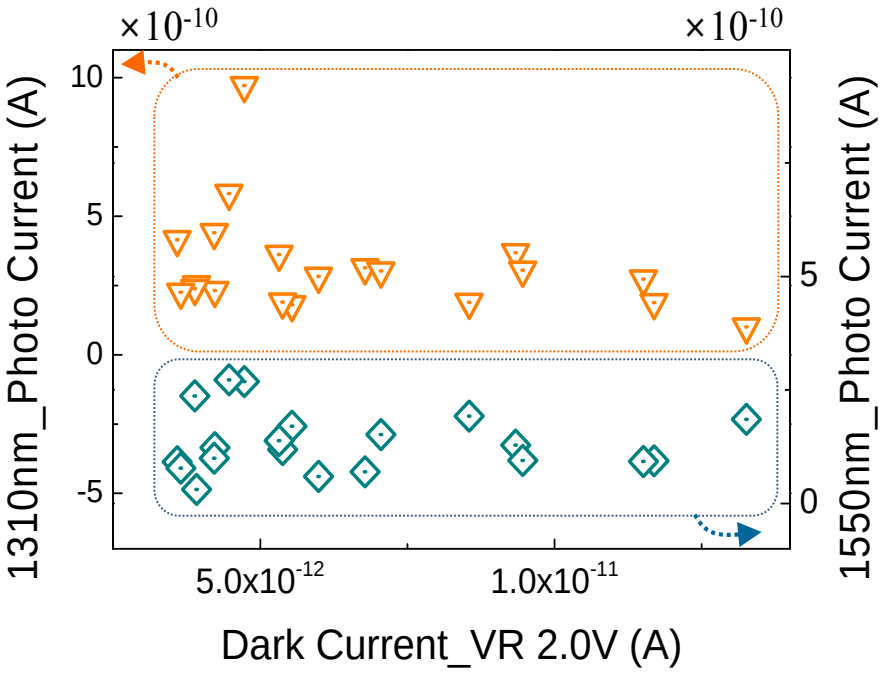

Fig. 3.13 Correlation plot of the photo generated currents by the FKE (triangle; 1310nm, rhombus; 1550nm) measured at the DC bias to give the fixed current level vs. the SRH leakage level for 20 different Zener diode samples. The photo current is measured at the DC bias to give the fixed current level.

Chapter 4

GIDL regime in the NMOSFET for IR detection

4.1 MOSFET as the photodetector of the infrared light

4.1.1 Energy band of the surface junction in the GIDL bias

To investigate the possibility of detecting IR by FKE, the device which is governed by tunneling mechanism, has been chosen NMOS like as the Zener diode of previous section. When the strong bias is applied between the gate and the drain, the scheme of GIDL biased MOSFET which has a depletion region at the surface junction is shown in Fig. 4.1 [50]-[51]. In the depletion region under strong uniform electric field, there can be the steep slope of the conduction band and the valence band. Tunneled states under strong electric field at GIDL surface junction can exist within forbidden band gap. As like the scheme shown in Fig. 4.2 for GIDL biased NMOSFET, electrons in the valence band may tunnel to the conduction band if the IR photon energy transfers for electrons of the valence band from A point in the forbidden gap followed by tunneling to B state in the conduction band state. The tunneling distance from A to B is $W = (Eg - \hbar\omega)/qF$, where Eg and $\hbar\omega$ are the bandgap energy and IR photon energy, respectively, and F is the electric field intensity, which is assumed to be constant between A and B in the Fig. 4.2 . As the tunneling current is dependent

on W in an exponential manner [46], photons of ħω (< Eg) may be detected if F is sufficiently large.

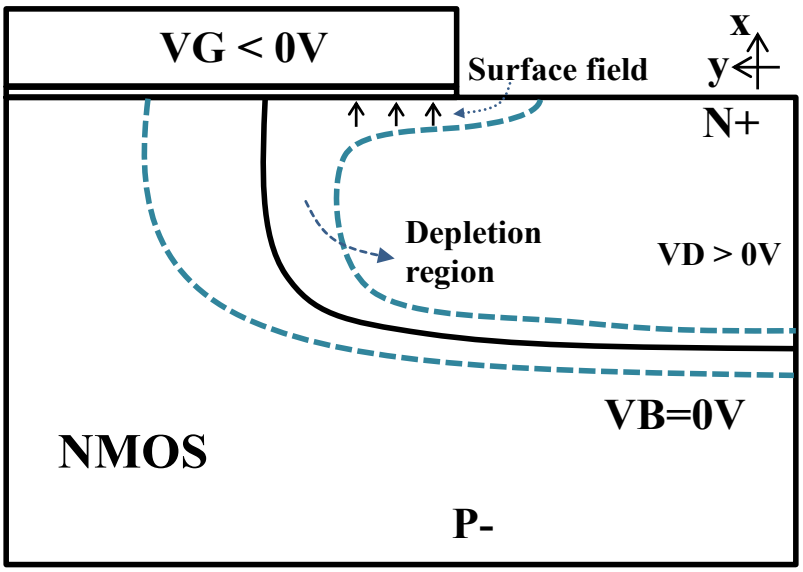

Fig. 4.1 Schematics of the MOSFET surface junctions under the GIDL bias condition

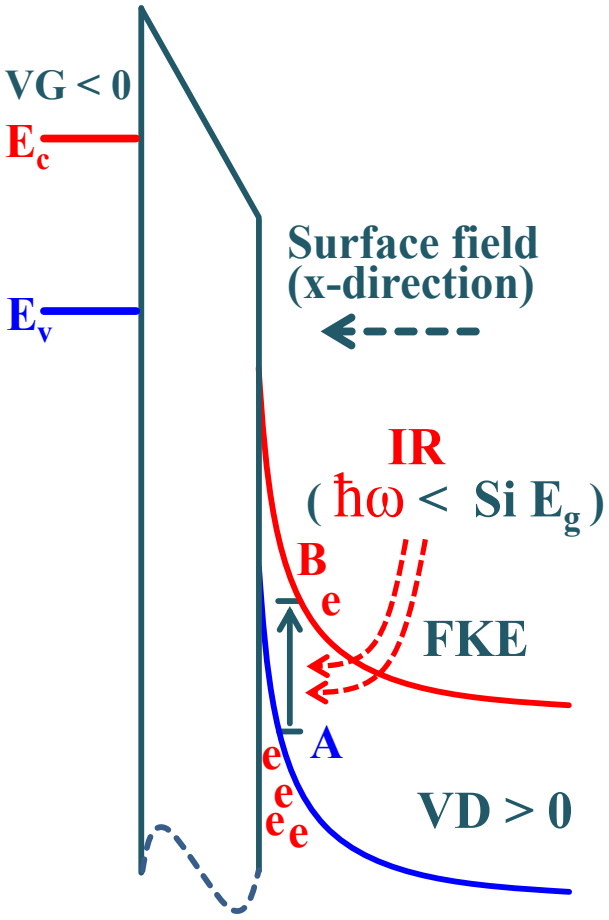

Fig. 4.2 Energy band diagrams under the GIDL bias conditions for the MOSFET, the FKE is used to detect the IR signal.

4.1.2 Structure of the NMOSFET test pattern

The second device considered in this work is an NMOSFET designed by our group with the following features; (1) the device has a large gate width in order to obtain large GIDL current, (2) Metal lines coverage on the junction should not block the incident light onto the surface junction. The structural image of the planar NMOSFETs is shown together with the microscopic image of the fabricated device in Fig. 4.6. To meet the consideration (1), the transistors form an array structure and shares the same gate, source and drain electrodes in Fig 4.3. The total effective width of the 200 array transistors is 2000μm in Fig. 4.4. The gap between the gate and the drain metal for the illumination of the infrareds is 2.5μm, which means effective window in both side of the gate as shown in Fig. 4.5.

In Fig. 4.6, the inset shows the gate line under gap-filled insulator of SiO_2. The bias condition for the GIDL measurement in which the same bias of 2V is applied to paired source and drain. The GIDL current flows from the common source and drain junctions to the Si body. The gate of the 180nm length is N+ polysilicon ($1.5x10^{20}cm^{-3}$). The doping concentrations of the P- substrate and the source/drain are $7.78x10^{17}cm^{-3}$ and $1.1x10^{20}cm^{-3}$, respectively. The gate spacer is made of Si_3N_4 with the thickness of 50nm and the gate oxide thickness is 3.9nm.

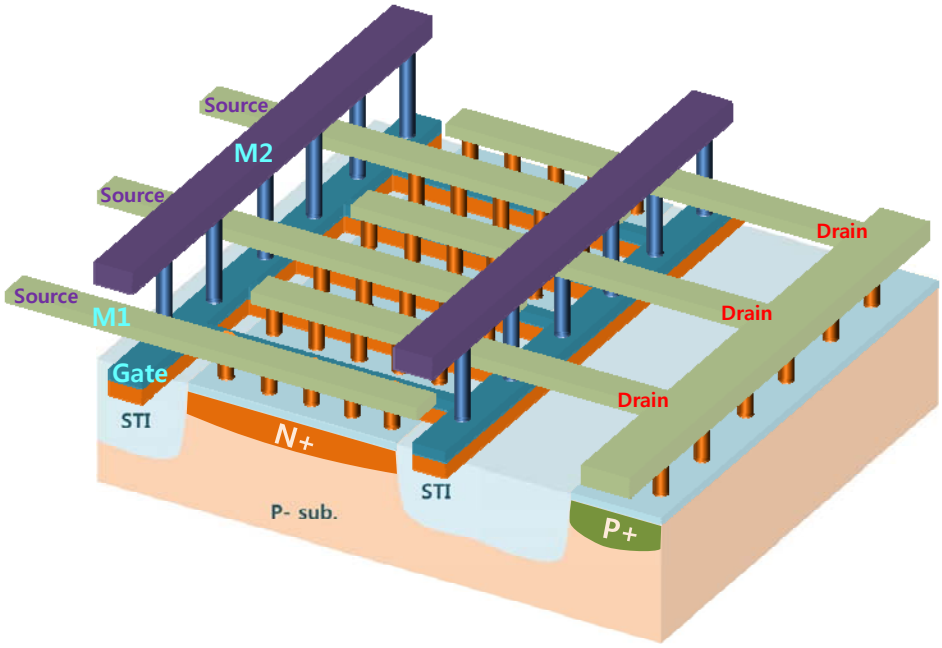

Fig. 4.3 Structural schematic image is shown 4-terminals of arrayed transistors are all connected to each one terminal pad.

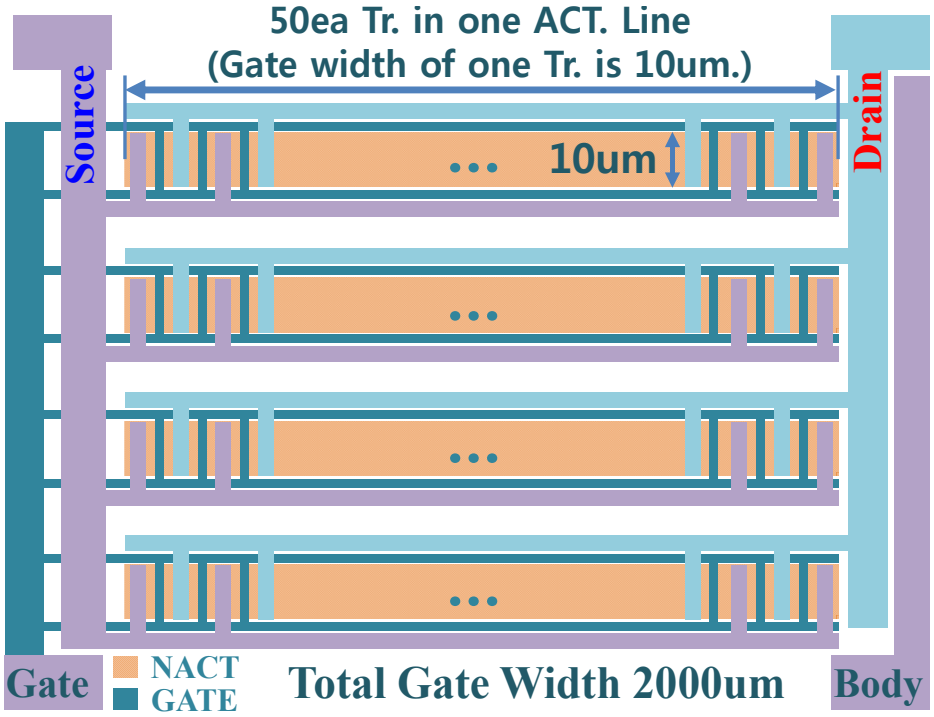

Fig. 4.4 Layout image of the NMOS, where the gate width is expanded up to 2000um.

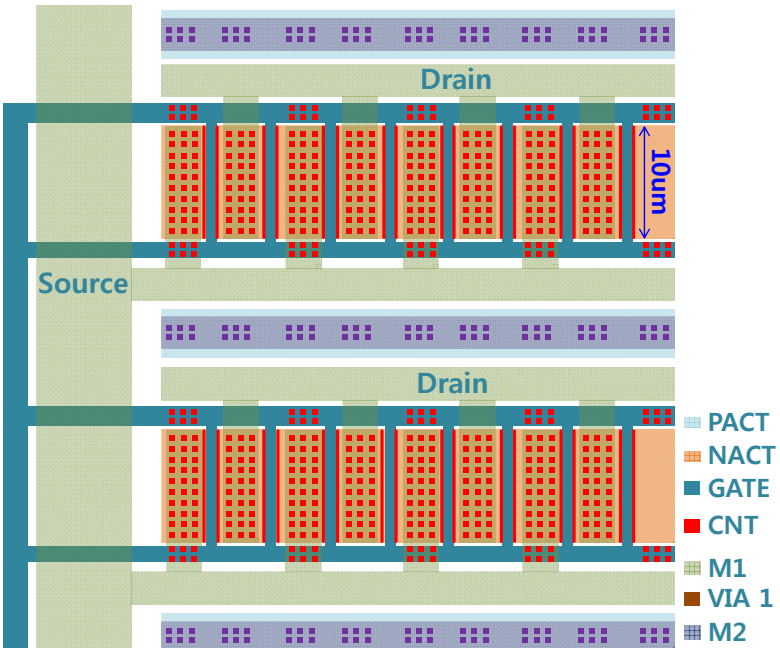

Fig. 4.5 Layout image of the NMOS, when paired the source and the drain is biased at GIDL condition, depletion region can be expanded to the both side of the gate. With the bias condition, the length of GIDL region is expanded up to 4000um.

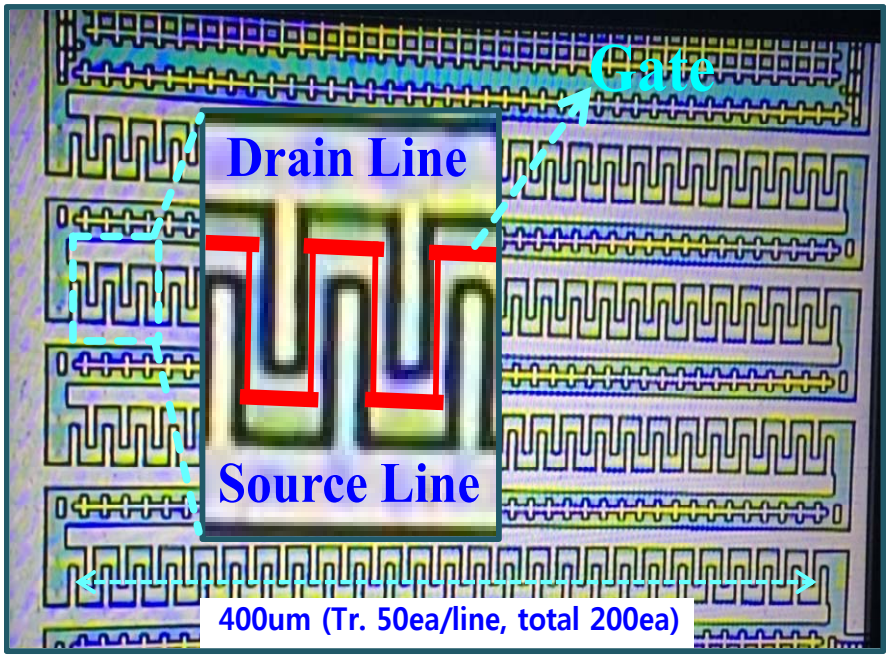

Fig. 4.6 Microscope image of the experimental MOSFET with the effective gate width of 2000μm. Inset; the effective window through which the light can be illuminated on the surface junction is shown.

4.2 DC Measurement results

4.2.1 Limitation of the photo sensitivity in the DC bias scheme

Using the NMOS, GIDL current is measured with DC bias of VD=VS=0.05V or 2.0V (paired) and VB=0V under 808nm, 1310nm and 1550nm of IR lasers as shown in Fig. 4.7. The measured GIDL current shows the increase by the illumination of IR lasers as the VG is swept up to -3V with fixed VD and VS as shown in Fig. 4.8. From DC mode measurement of Fig. 4.8, photo generated current under 808nm, 1310nm and 1550nm of IR through the subtraction from dark current, is plotted with demonstrating the bias dependency for all IR lasers except of 808nm (having larger energy than silicon band gap energy) with the meaning of the generation by FKE as shown in the Fig. 4.9. When paired source and drain of 0.05V is low, the photo generated current under 1550nm of infrared shows no bias dependency even though the gate bias is increased up to -2.0V. For the case of 1310nm, 808nm lasers, the photo generated current has shown flat gate bias dependency at even up to -3V. This is due to that flat photo generated current under 1310nm and 1550nm of lasers has the transition mechanism through traps. To get reasonable FKE current, it needs to be stronger bias to the GIDL junction. Thus, when paired source and drain bias is increased to 1.0V, the photo generated current under 1310nm starts to be shown the bias dependency. However, the responsivity shows so small that is necessary to be increased. Thus, paired source and drain bias is increased up to 2.0V and the gate bias is swept from 0V to -3V as shown in the Fig. 4.10. As the result of the measurement, the photo generated current under 1310nm and

1550nm of infrareds is resulted showing of 20.14 ㎂ and 25.86 ㎂, respectively. The responsivities under 1310nm and 1550nm of infrareds which has the optical power 5mW and 10mW are shown 0.00404 and 0.00259A/W, respectively at the Fig. 4.11. Table 4.1 shows arranged the measurement result of the responsivity under 808nm, 1310nm and 1550nm. Although the VDG (Gate to Drain bias voltage) is increased up to DC 5V to increase reasonable responsivity under 1310nm and 1550nm of infrared, the responsivity has been in the ungratified states in DC mode. Therefore, although the VG should increase more and more in order to obtain high reasonable responsivity, the VG has the bias limit only up to -3V in DC mode due to the gate insulator break down.

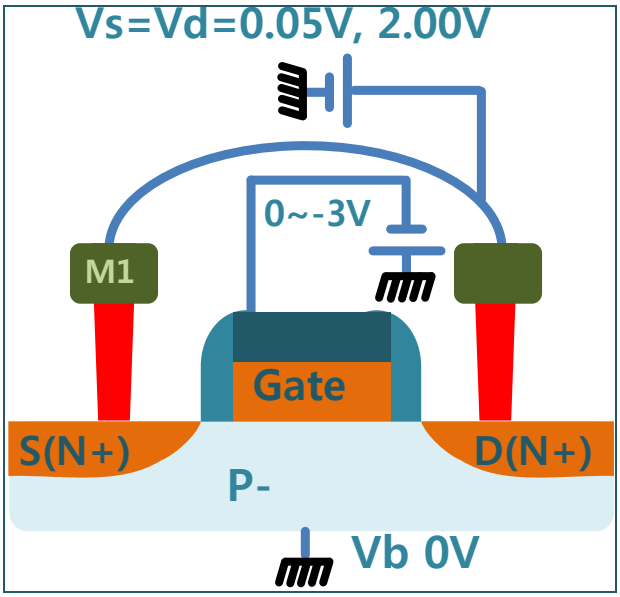

Fig. 4.7 DC bias scheme for the GIDL current measurement. VG varies 0 ~ -3V with fixed voltage 0.05V and 2.0V applied to both source and drain. In this way, the GIDL region can be located at both surfaces of the source and the drain.

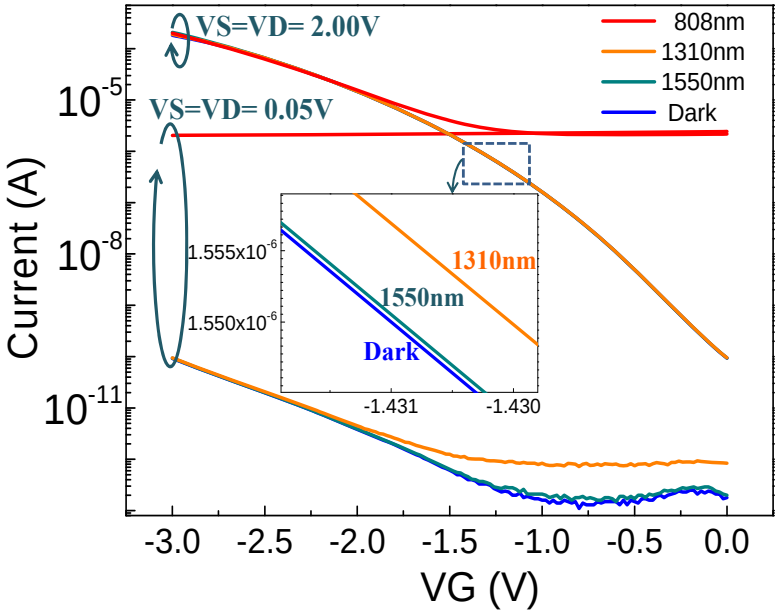

Fig. 4.8 GIDL current vs. VG (DC condition up to -3V) of the NMOSFET under the DC bias of VD=VS= 0.05V or 2.0V (paired) and VB=0V under the illuminations with 808, 1310 and 1550nm.

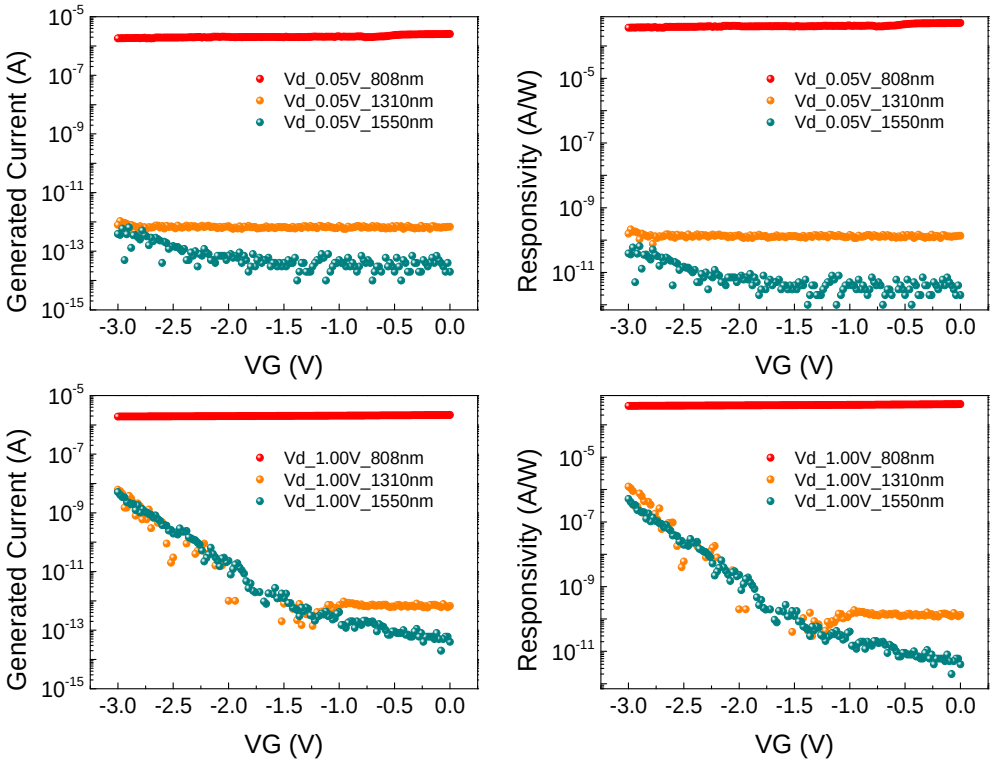

Fig. 4.9 Photo generated current vs. VG (both the DC mode up to -3V and pulsed mode up to -6.8V) with paired source and drain of 0.05V and 1.0V under the illuminations of 808, 1310 and 1550nm.

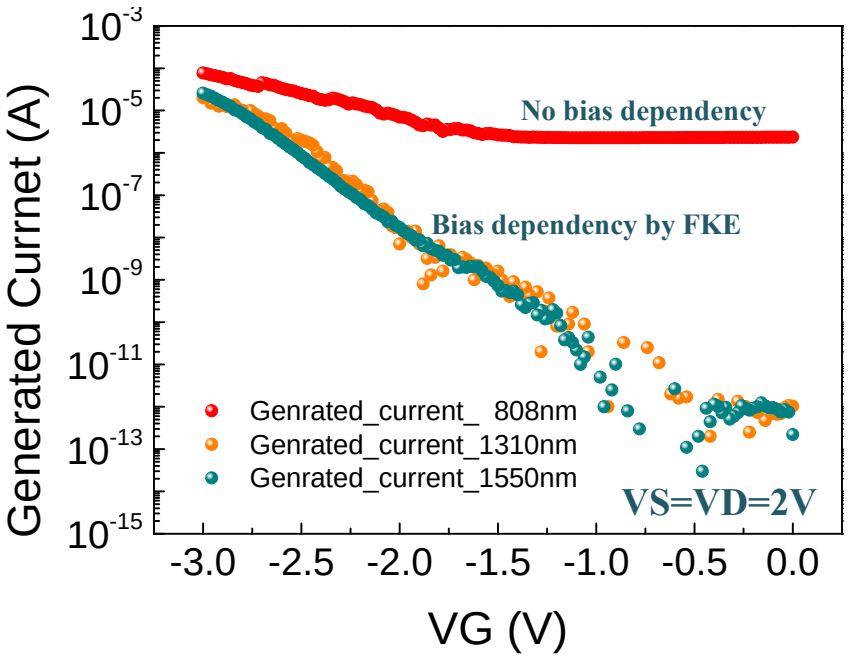

Fig. 4.10 Photo generated current vs. VG (DC condition up to -3V) under the illuminations with 808, 1310 and 1550nm.

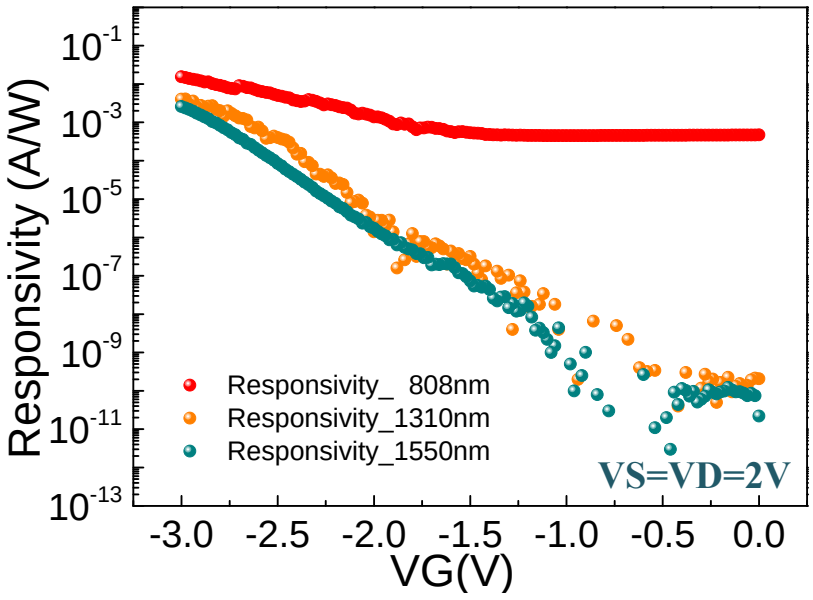

Fig. 4.11 Responsivity vs. VG (DC condition up to -3V) under the illuminations of 808, 1310 and 1550nm

	808nm	**1310nm**	**1550nm**
Generated current (uA)	76.89	20.14	25.86
Optical Output Power (mW)	5.0	5.0	10.0
Responsivity (A/W)	0.01538	0.00403	0.00259

Table 4.1 Responsivities of the Zener diode under 808nm, 1310nm, and 1510nm infrareds by the DC bias measurement

4.3 Pulsed bias scheme to induce the NMOS GIDL

4.3.1 Circuit diagram for the pulsed bias scheme

In previous section, the photo sensitivity is needed to increase with DC measurement. However, there is the DC bias limit due to the gate insulator breaking. This DC bias limit bothers to increase infrared photo responsivity by Franz-Keldysh effect.

In order to overcome this limit of DC bias which is mentioned, more sparsely patterned pulse (with a 50μs pulse peak for every 0.2s) than patterned pulse for the Zener diode has been applied to avoid a constraint; the gate oxide breakdown caused by the high electric filed between the gate and the drain. It should be noticed that the oxide breakdown is determined by the total influence of electron carrier tunnel through the oxide [57]-[59]. In this experiment, the laser source has been biased with the pulsed synchronized with the sensor even the IR signal does not have to be synchronized with the photo-receiver in the real applications. Vin+ of OP amplifier is biased of 2V to paired source and drain in order to make the condition of GIDL current in the circuit for NMOS of Fig. 4.12. Additionally, the pulse width of 50μs is chosen to be long enough for the junction to reach the steady state needed to maintain the FKE. In the next section, the experimental results from MOSFET are described in detail.

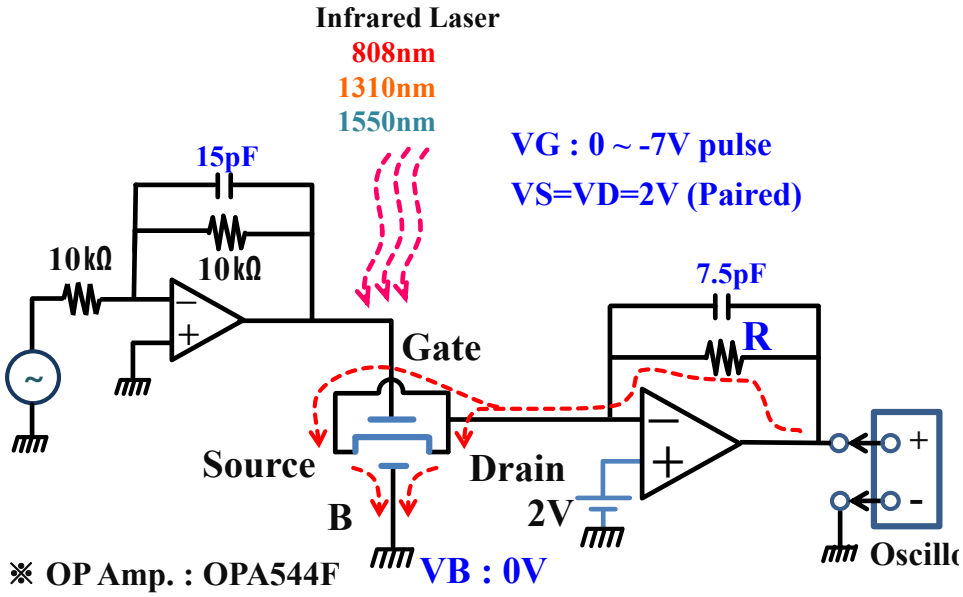

Fig. 4.12 The circuit diagram used to apply the pulse bias to NMOSFET, the left OP amplifier circuit is to avoid the overshoot voltage from the pulse generator. The GIDL current is measured by the silicon substrate current.

4.3.2 Current response to the pulsed wave

As explained in previous section, generated pulses are applied to the gate using the circuit. Figure 4.13 shows more sparsely patterned pulse (with a 50μs pulse peak for every 0.2s) than patterned pulse applied for the Zener diode. Sparsely patterned pulse with 50μs is applied to the gate with the pulse amplitude from 0V to -6.8V. Amplitude of the gate pulse is applied by -3V has shown in Figure 4.13 as an example. And Figure 4.13 also shows the measured output voltage which means the photo response by infrareds when the pulse is applied. As shown in Fig. 4.13, the photo generated current is calculated by extracting the delta voltage from the output voltage caused by dark conditions and the photo response. Additionally, the output voltage of the steady state is chosen for calculating the photo generated current to maintain the FKE sufficiently.

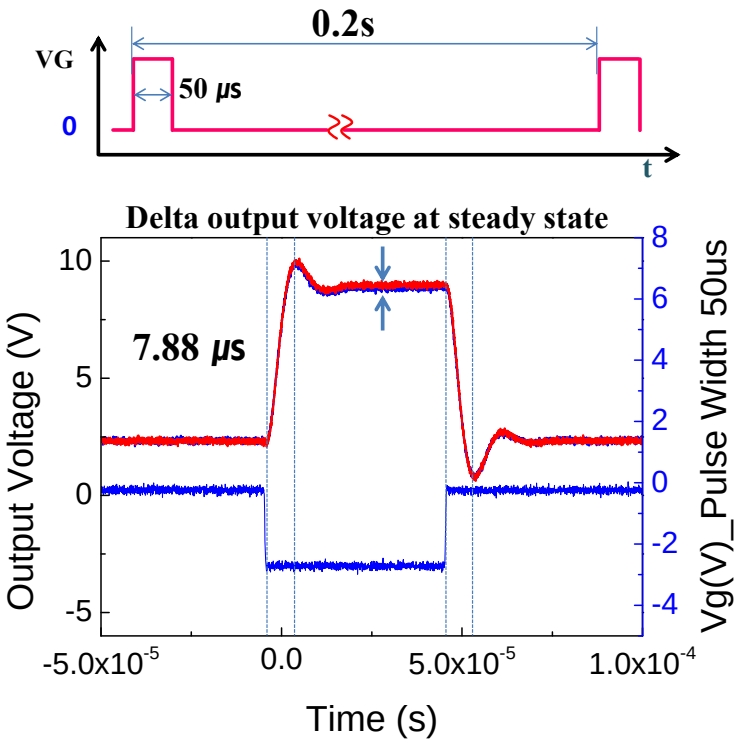

Fig. 4.13 Responsivity vs. pulsed bias voltage under the illuminations with 808, 1310 and 1550nm

4.4 IR photo response under the pulsed bias scheme

In previous section, using the NMOS, GIDL current was measured with a DC bias under the 808 nm, 1310 nm, and 1550 nm IR lasers. The measured GIDL current shows an increase as a result of the illumination of IR lasers as the VG is swept up to -3 V with fixed VD and VS. From the DC mode measurement, photo generated current under 808 nm, 1310 nm, and 1550 nm IR is plotted with bias dependency. However, the responsivity for the 1310 nm and 1550 nm IR lasers is in ungratified states at the VG of -3 V in DC mode. Although the VG should progressively increase in order to obtain high reasonable responsivity, the VG has a maximum bias limit of -3 V in DC mode owing to gate insulator break down. Accordingly, the pulsed bias is given for the VG with a fixed VD of 2 V (with the pair of VS) under illumination with IR lasers. The measured photo generated current and the responsivity in pulse mode are also shown together with the DC measurement in Fig. 4.14.

In the case of the pulsed bias, we applied a maximum V_G of -6.8 V *(*one 50 μs pulse for the duration of 0.2 s). The bias condition was sufficiently large to induce an FKE effect (which was also verified through computer simulation). Thus, responsivities as high as 0.484, 0.0362, and 0.0178 A/W were obtained for the 808, 1310, and 1550 nm infrared lasers, respectively, as shown in Fig. 4.15. The responsivity was calculated to be as small as two orders of the Zener diode under the same IR conditions, which may be understood to be as a result of lack of the avalanche multiplication that is present in the case of the Zener diode. The situation may be improved if a large negative substrate bias is applied to cause a multiplication.

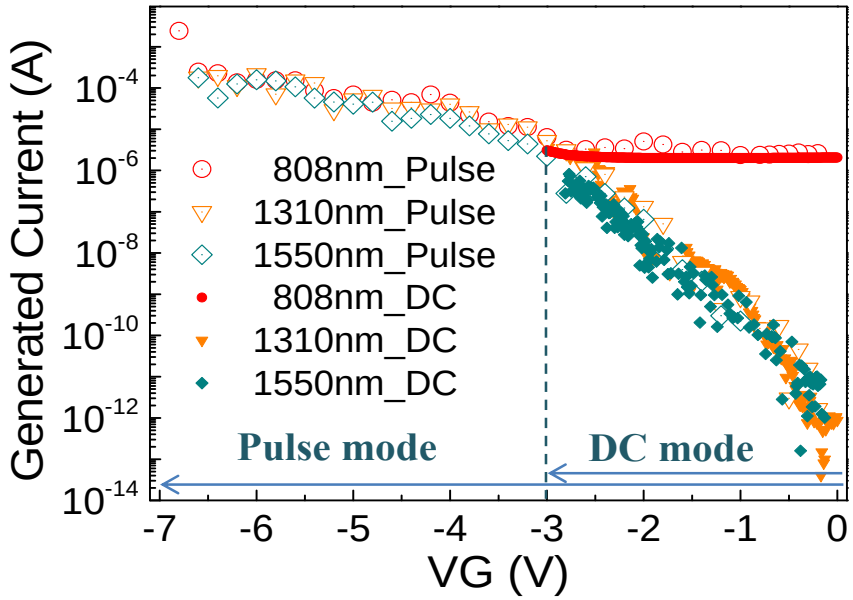

Fig. 4.14 Photo generated current vs. VG (both the DC condition up to -3V and pulsed condition up to -6.8V) under the illuminations with the light sources of 808, 1310 and 1550nm.

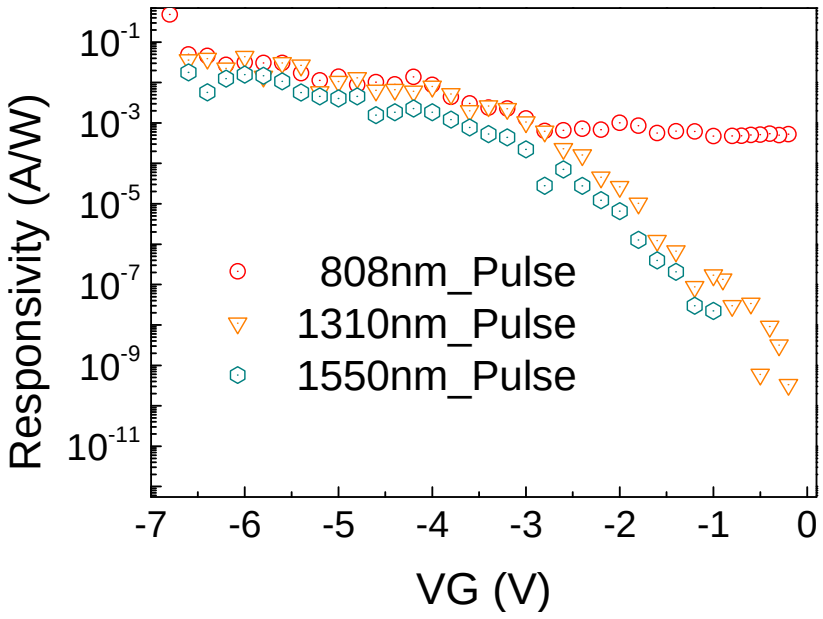

Fig. 4.15 Responsivity vs. pulsed bias voltage under the illuminations with 808, 1310 and 1550nm

Chapter 5

Multiplication of IR signal with NMOSFET

5.1 Multiplication of the FKE current

5.1.1 Schematics of the multiplication of FKE current

In previous chapter, the measurement of the photo responsivity is performed under GIDL only mechanism by vertical electric field. The photo responsivity under the infrared with the NMOS is little bit lower than the Zener diode case due to the lack of the avalanche multiplication of the photo generated current. In order to overcome low photo response of the NMOS, the enhancement of the photo response is intended using different bias scheme in this section.

When the strong substrate bias is applied negatively with GIDL bias measurement conditions as shown in Fig. 5.1, it is tried to increase the lateral electric field in the GIDL surface junction. When the strong substrate bias is applied to negatively, depleted region of the NMOS body and the surface junction is expanded and increased as shown in Fig. 5.1 [60]-[62]. Of course, as well as GIDL tunneling current due to the surface electric field, it is possible to expect a multiplication of the GIDL current because the lateral electric field

also increases. Figure 5.2 shows a scheme for the multiplication of the GIDL current and the GIDL current itself. The photo current generated by Franz-keldysh effect under the illumination of infrareds at the surface junction will be able to expect the multiplication by the impact ionization finally when the strong bias of the substrate is applied negatively.

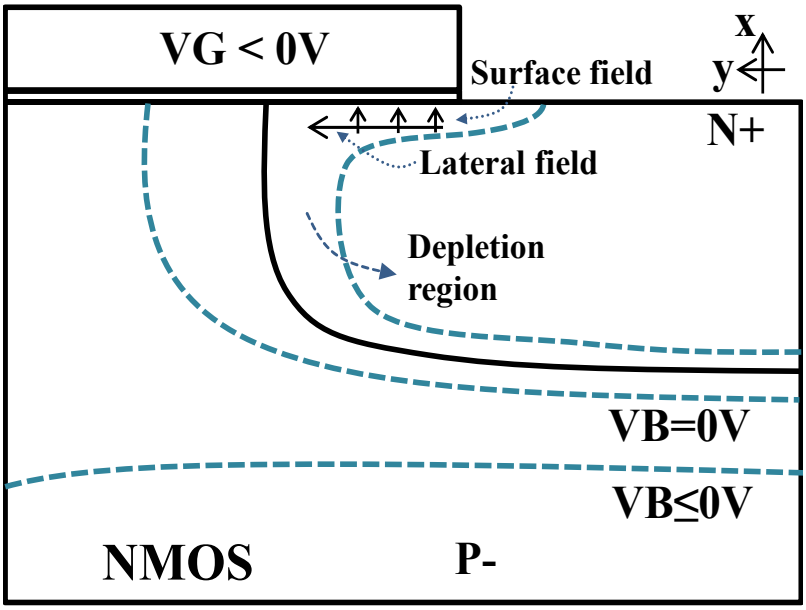

Fig. 5.1 Schematics of the MOSFET surface junctions with lateral electric field which is added by negative substrate bias.

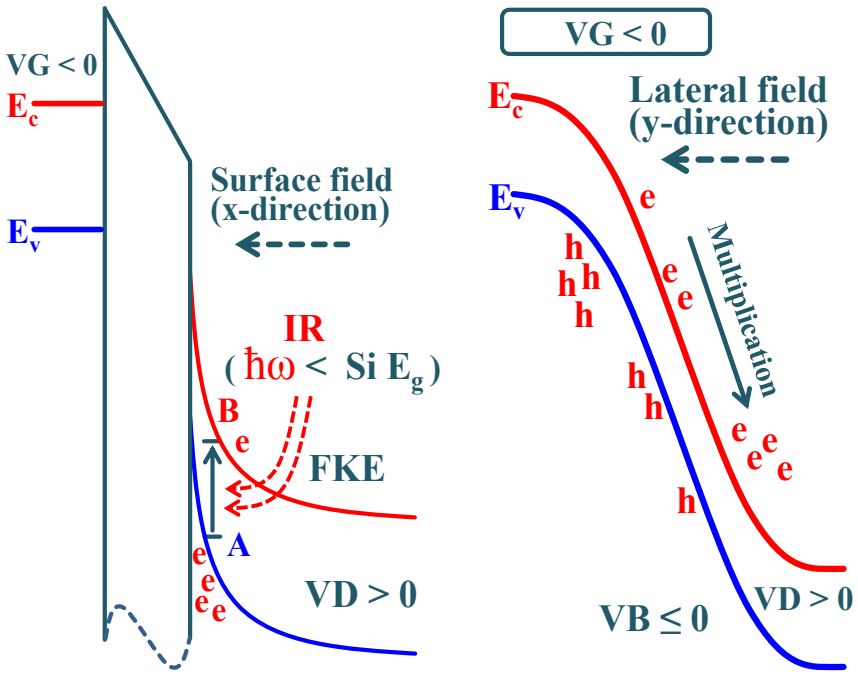

Fig. 5.2 Energy band diagrams in the FKE bias conditions for the FKE +GIDL bias conditions for the MOSFET. When the Si substrate is biased negatively, the photo current can be multiplied.

5.2 Results of DC Measurement

5.2.1 Multiplication by the substrate bias

Using the NMOS, paired source and drain current vs. the substrate bias with fixed the gate bias split (0V, -1V, -2V, -3V) in DC mode (VD=VS=2V) under dark at room temperature as shown in Fig. 5.3. As the substrate bias increase negatively, the lateral electric field increases at the surface junction of the NMOS. Thus, as the substrate bias increase with fixed the gate bias split of 0V - -3V, the paired source and drain current is plotted with small increase of substrate bias dependency up to the substrate bias of -10.2V. When the gate bias field increases, the GIDL current is also shown as the increased level. At the regime of breakdown voltage above -10.2V, Fig. 5.4 shows the characteristics that the breakdown voltage decreases as GIDL surface electric field increases explaining the multiplication of the GIDL current. As explained in previous section, through the multiplication of the GIDL which is induced by the increase of the substrate bias, photo generated current is expected to be multiplied to enhance the photo responsivity like as the Zener diode case. When the gate bias is swept with the substrate bias split (0V, -6V ~ -13V) which means lateral tunneling current increase by lateral electric field. As shown in the Fig. 5.5, GIDL current has the substrate bias dependency of lateral tunneling current. In summary for this section, when the substrate bias is increased, two additional current mechanisms can be added; (1) the multiplication of GIDL current, (2) lateral tunneling current by lateral electric field.

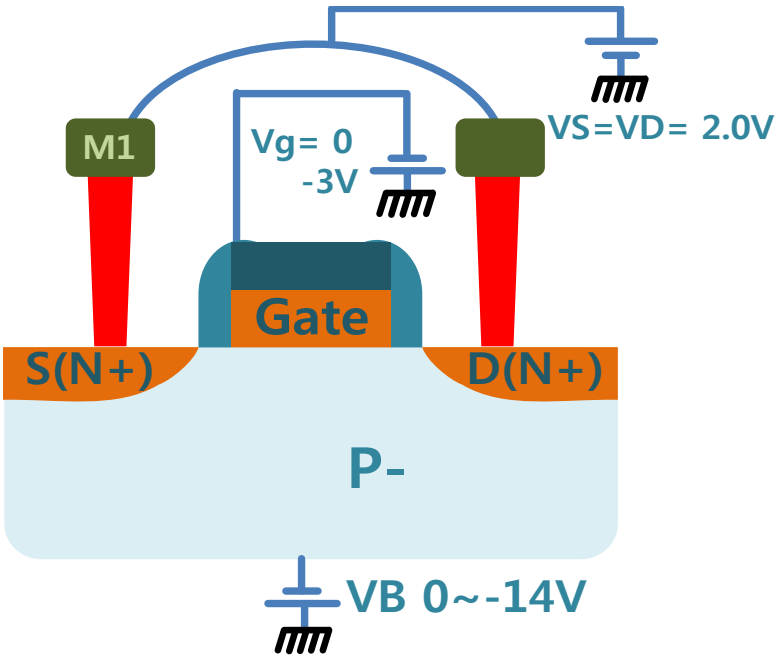

Fig. 5.3 DC bias scheme of the Si substrate to multiply the photo current

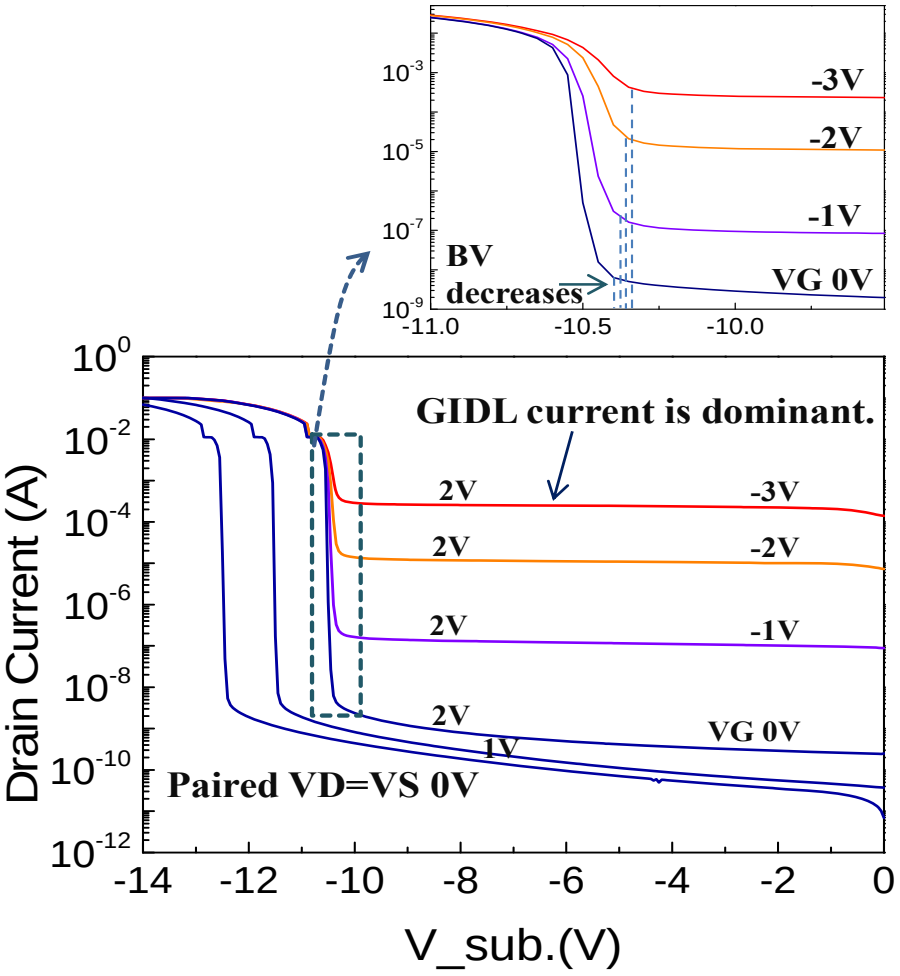

Fig. 5.4 Paired source and drain current vs. the substrate bias with fixed the gate bias split (0V, -1V, -2V, -3V) in DC mode (VD=VS=2V) under dark at room temperature.

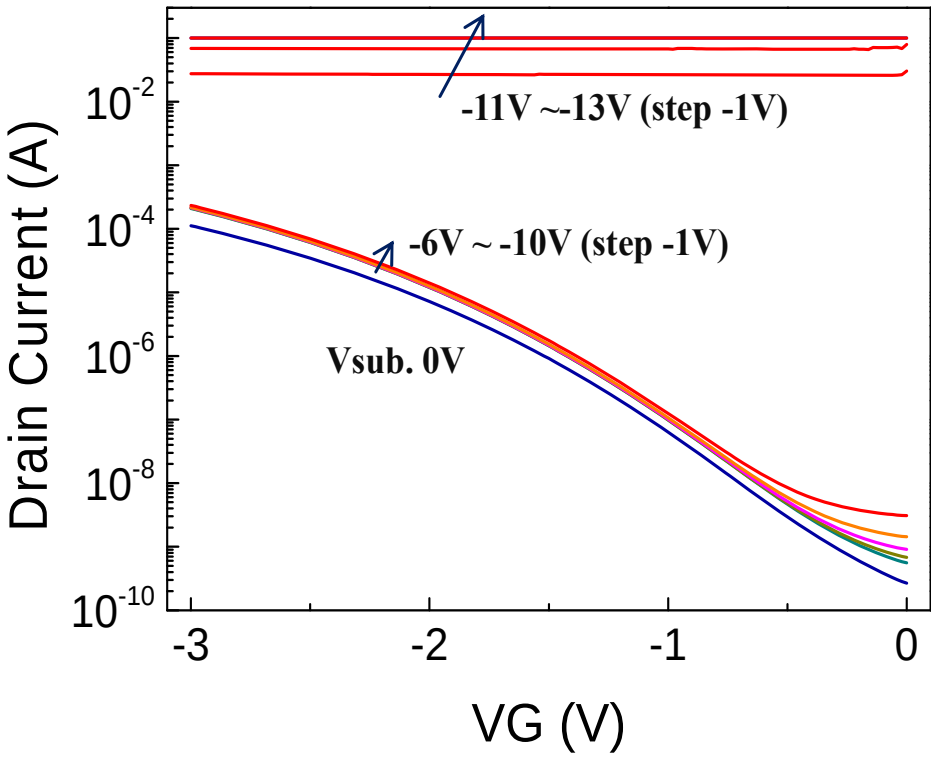

Fig. 5.5 Paired source and drain current vs. the gate bias with fixed the substrate bias split (0V, -6V~-13V with the step of -1V) and the source drain voltage (VD=VS=2V) under the dark condition at room temperature.

5.2.2 Temperature dependency

Prior to first measurement of photo generated current by infrareds, the temperature dependency of the current is measured in a dark state. As the substrate bias increases for the NMOS, the temperature coefficient was measured to investigate current mechanism like in the case of the Zener diode. The measurement conditions were described as fixed DC 2V for the paired source and drain and -1, -2 and -3V for the gate bias. For the substrate, DC bias was sweep from 0 to -14V. For this measurement, the temperature is going up from 45℃ to 85℃ with the step of 20℃ to measure the paired source and drain current.

For the result of temperature dependency measurement, below the breakdown bias, the measured result shows the reverse leakage current when VG = 0V, in the next, when VG is increased from -1 to -3V, current level is also increased showing the temperature dependency at Fig. 5.6. This is well matched the positive temperature coefficient of the reverse leakage current and GIDL tunneling current as shown in previous result of the Zener tunneling. However, the negative temperature coefficient is shown at the regime of breakdown bias. That is the crucial evidence for the multiplication of the GIDL current which is reduced as the temperature increases. In other words, GIDL current by substrate bias supports to be multiplied by impact ionization as in the case of a negative temperature coefficient of Zener diode.

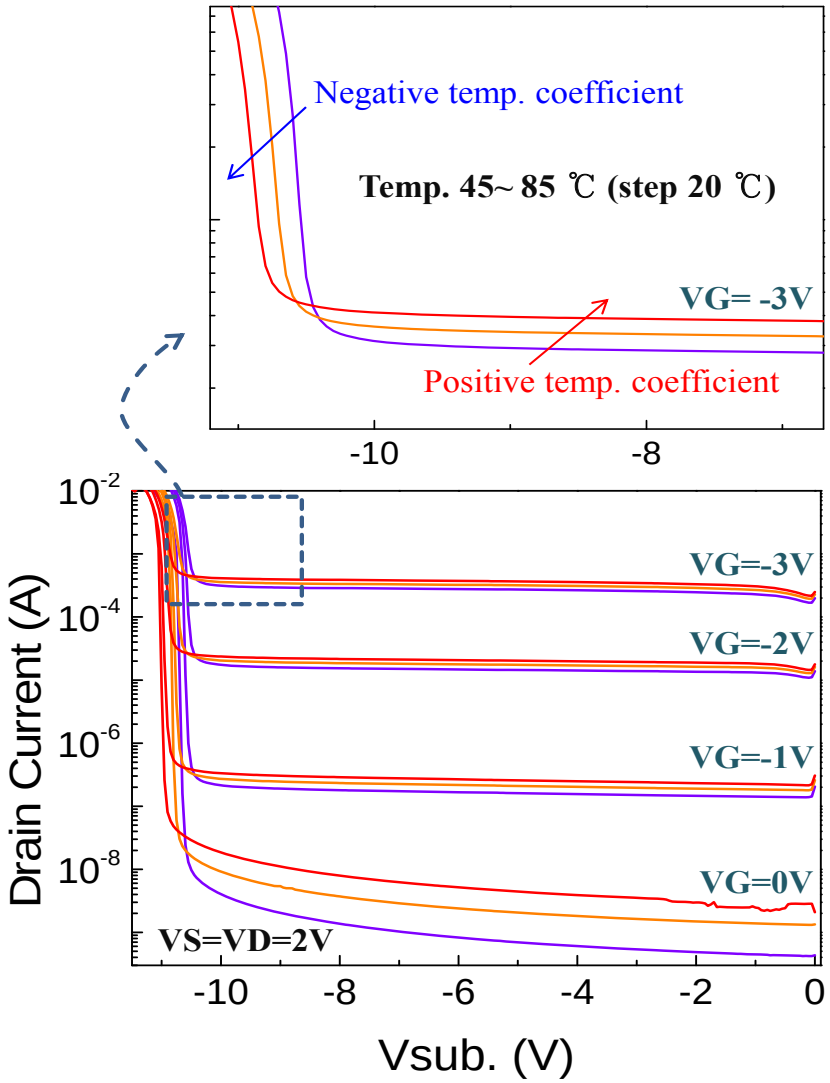

Fig. 5.6 Paired source and drain current vs. the substrate bias with fixed the gate bias split (0V, -1V, -2V, -3V) in DC mode (VD=VS=2V) under the dark condition with the temperature split from 45℃ to 85℃ with step 20℃.

5.2.3 Degradation in the photo sensitivity

At first, based on the information discussed in the previous section, this section is intended to find out the photo response by the infrared through the DC measurement. For the bias condition, the substrate bias was swept from 0V to -14V with paired VS = VD = 2V, and also fixed VG = -1V, -2V, -3V. In the DC bias conditions, it was measured under the dark and 1310nm infrared irradiation conditions. Fig. 5.7 shows the measured current of paired source and drain current displaying a current difference between the dark state and 1310nm infrared on state. From the measured value, a photo generated current is plotted as shown in Fig. 5.8. Up to the substrate bias of -10V, photo current has been well generated. However, as the substrate bias is increased more than -10V, photo generated current shows smaller or negative value than that in a low bias range of substrate. Additionally, differences are appeared as the gate voltage is swept from 0V to -3V while paired VS = VD = 2V was fixed and -6V, -8V, -10V, -12V of the substrate was split as shown in Figure 5.9. As the gate bias is increased to measure, the result of the GIDL current seems to be increased with the substrate bias under the 1310nm infrared. The plot of the photo generated current by FKE in Fig. 5.10 with increased VG shows the state also increased. However, at stronger gate voltage regime than -2.5V, the photo current shows the degradation. The substrate bias is also seen as dominant role that the photo generated current has more significant reduction. It seems a negative temperature coefficient of the avalanche multiplication by the impact ionization is caused by the Joule heating due to the substrate bias. In order to increase the photo response, the degradation of the photo generated current should be enhanced. In order to increase the photo responsivity, the usage of pulsed bias

scheme and the result of a pulsed measurement will be referred in the following section.

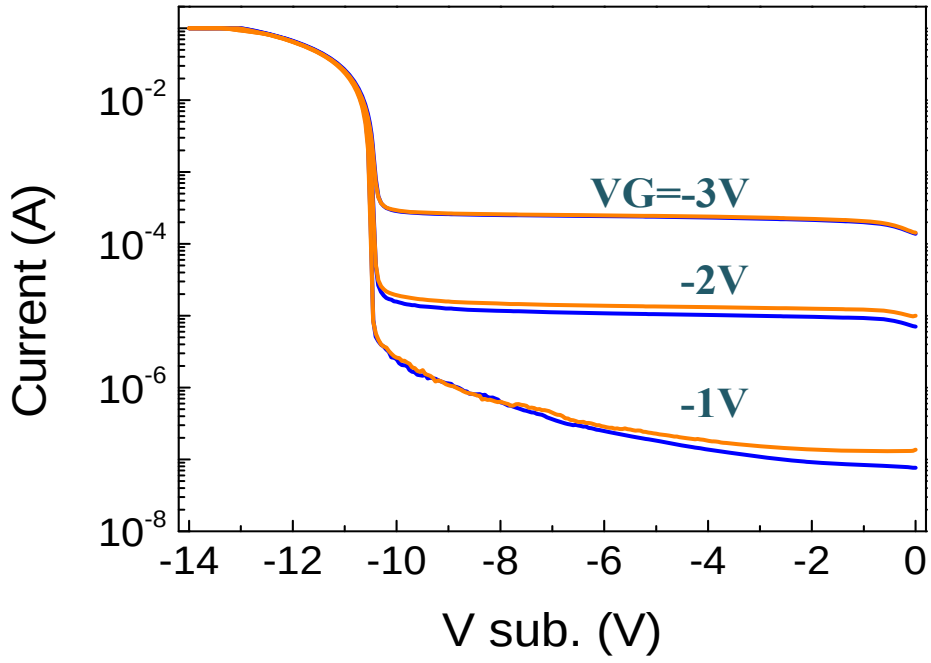

Fig. 5.7 Paired source and drain current vs. the substrate bias with fixed the gate bias split (-1V, -2V, -3V) and the DC mode (VD=VS=2V) under the dark and the 1310nm infrared conditions.

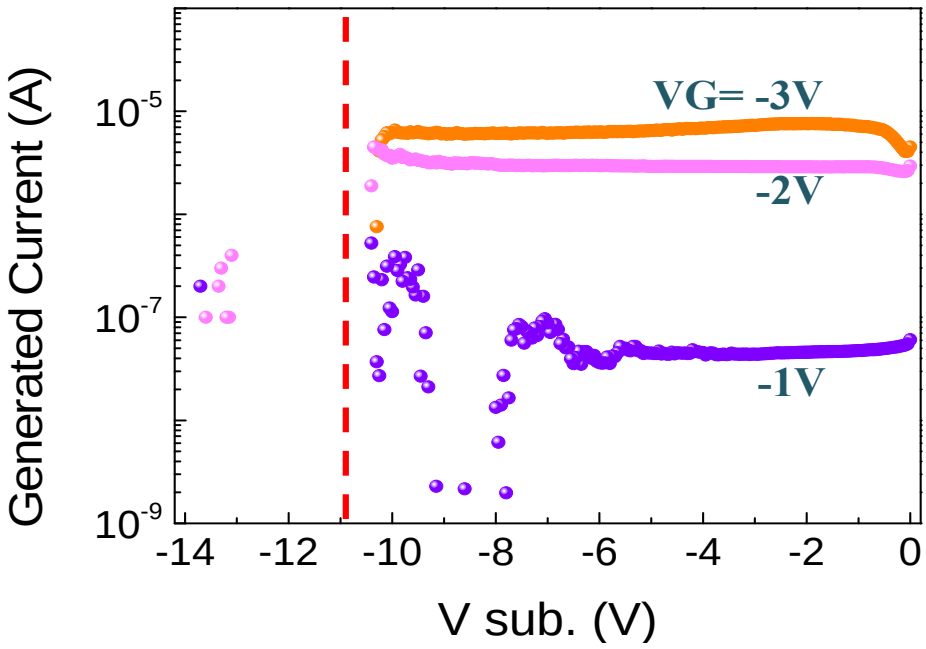

Fig. 5.8 Paired source and drain current vs. the gate bias with fixed the substrate bias split (-6V, -8V, -10V and -12V) in DC mode (VD=VS=2V) under the dark and the 1310nm infrared conditions.

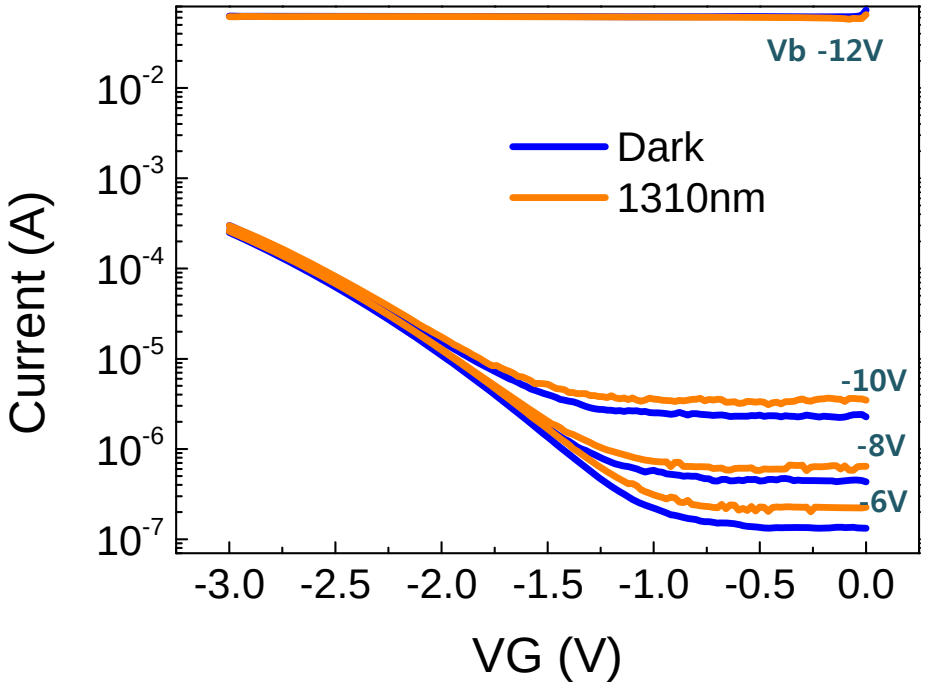

Fig. 5.9 Paired source and drain current vs. the gate bias with fixed the substrate bias split (-6V, -8V, -10V and -12V) in DC mode (VD=VS=2V) under the dark and the 1310nm infrared.

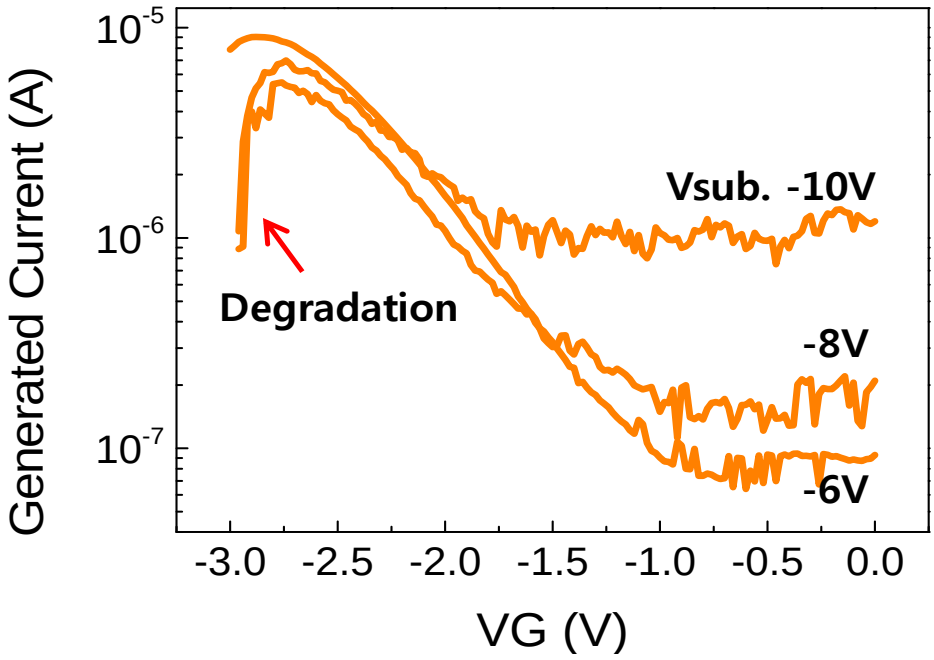

Fig. 5.10 Photo generated current vs. the substrate bias with fixed the substrate bias split (-6V, -8V, -10V) in DC mode (VD=VS=2V) under 1310nm infrared. Photo current shows the degradation as the substrate bias increases.

5.3 Pulsed bias scheme

5.3.1 Circuit diagram for pulsed bias scheme

In the case of NMOSFET, more sparsely patterned pulse (with a 50μs pulse peak for every 0.2s has been applied to avoid a constraint; the gate oxide breakdown caused by the high electric filed between the gate and the drain. Additionally, for the multiplication of the photo generated current by FKE, negative temperature effect must be considered when photo generated current is followed by the multiplication applying strong bias to the substrate the same as in the case of Zener diode. Thus, pulsed bias scheme is necessary for this experiment. However, the pulse generating circuit as shown in Fig. 5.11 is different from that of GIDL mechanism only in the previous section. The significant difference is the point that two synchronized pulses are applied to the gate and the substrate. The amplitude of two synchronized pulses has been composed with fixed -3V for the gate and swept from 0V to -14V for the substrate. At the same time, DC 2V has been applied for paired source and drain to satisfy the GIDL bias conditions. Under this bias condition, the input pulse is applied to the gate and the substrate using the circuit, the investigation is performed to measure the output voltage with an oscilloscope as the photo response under 1310nm and 1550nm of infrareds. Let's look for the input & output pulse for the measurement in the next section.

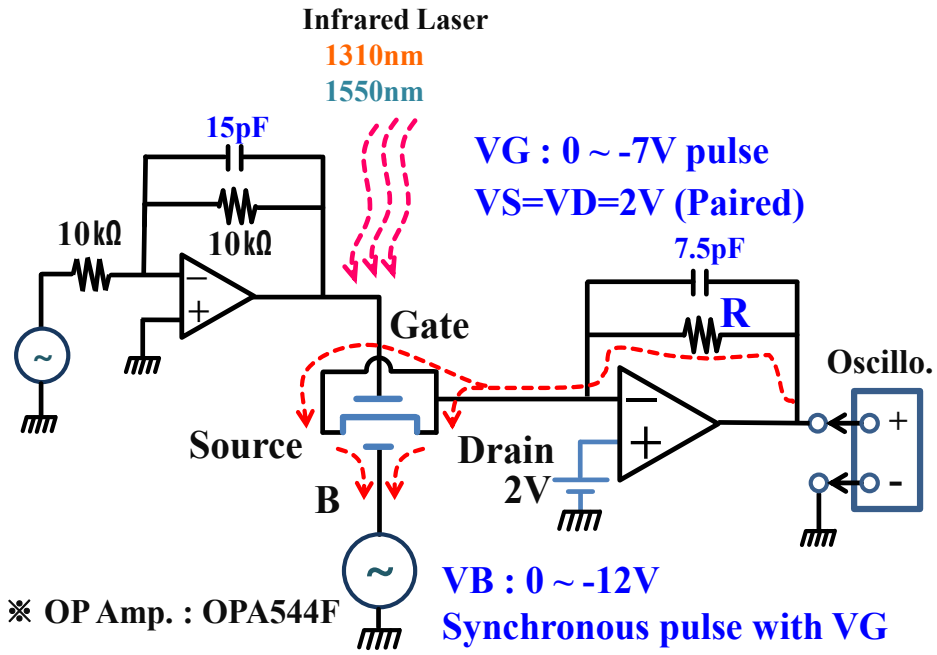

Fig. 5.11 Circuit diagram for the gate and the substrate to generate GIDL current and the multiplication of GIDL current

5.3.2 Response to the input pulsed wave

The generated pulse is applied to the gate and the substrate using the circuit in the previous section. Fig. 5.12 shows two input pulses. The width of the synchronized pulse is applied to 50μs for the gate and the substrate. By the way, fixed pulse amplitude of -3V for the gate and 0 ~ -14V for the substrate are applied to sweep. Figure 5.12 shows an example of the pulse amplitude of -10V is applied for the substrate. In addition, more sparsely patterned pulse (with a 50μs pulse peak for every 0.2s) has been applied to avoid constraints; (1) the gate oxide breakdown caused by the high electric filed between the gate and the drain, (2) negative temperature effect is caused by the heating of a strong bias as mentioned in previous section. Fig. 5.13 shows measured output voltage of the pulse at the time of photo response. As shown in Fig. 5.13, the difference between the output voltages caused by dark conditions and the photo response is calculated to be the delta output voltage.

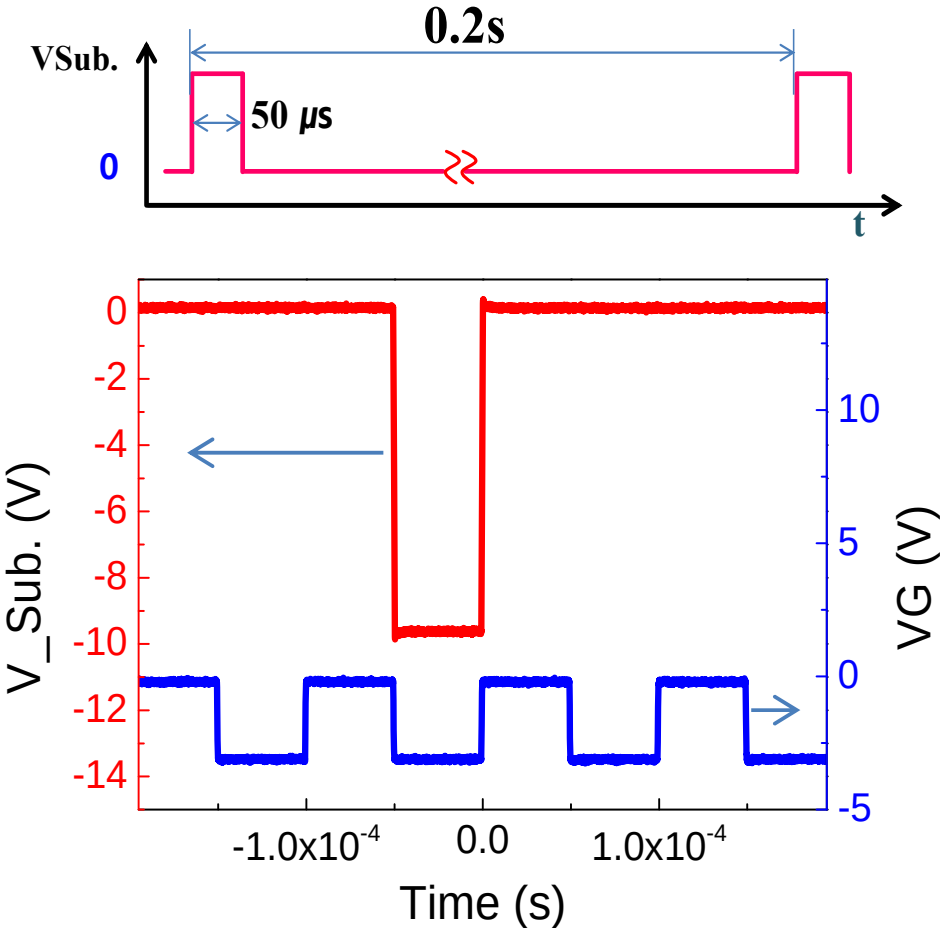

Fig. 5.12 Input pulsed wave to generate the gate and the substrate is shown. Synchronized pulse for the gate and the substrate have the GIDL bias and the multiplication of GIDL current.

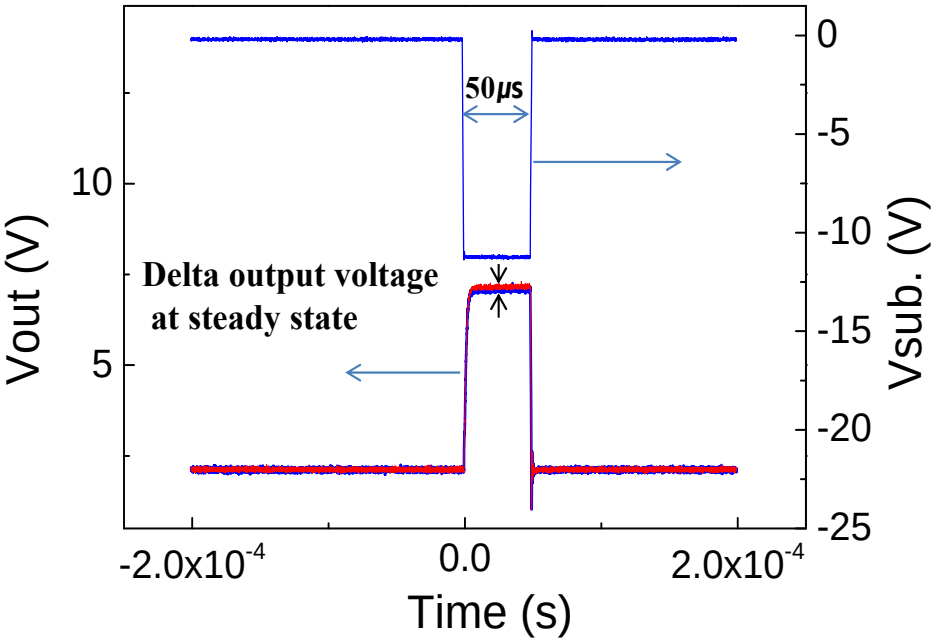

Fig. 5.13 Output voltage in accordance with the infrared laser switching on/off is shown. The difference is the delta voltage.

5.4 Enhanced response by the multiplication

The discussion is related to the effects of the avalanche multiplication in the MOSFET device in this section. As shown in Fig. 3.2, the avalanche effect from the carriers generated by the FKE is a natural consequence of PN field in the case of the Zener diode. That is not the case for the NMOSFET. As shown schematically in Fig 5.2, the electrons and holes generated by the FKE do not undergo the same electric field during excursion to the contact regions the 'avalanche multiplication' may not be obtained in the case of MOSFET. In order to see the potential of the impact ionization following the FKE generation in the case of NMOSFET, we modulate the substrate bias to heat up the FKE carriers (in the case of NMOSFET, holes are heated by during excursion to the substrate). Fig. 5.14 shows the resultant current as the bias of the substrate changes, while the VGD (Gate to Drain bias) is fixed. In order to avoid the junction heating effect as the Zener diode case, we applied pulsed bias for the substrate and the gate synchronously with the illumination of 1310nm and 1550nm of IR lasers. As shown in Fig. 5.15 where the responsivity vs. the pulsed substrate bias is plotted, the responsivity of as much as 0.318 and 0.105A/W has been obtained for 1310 and 1550nm infrareds radiation, respectively. Despite of relatively low VG (fixed to -3V), appreciable responsivity has been obtained as the results of the impact ionization current from the FKE generated electrons and holes. As the final discussion, the results have been obtained from the conventional planar structured NMOS, where the FKE generation region is confined to very shallow surface junction regions.

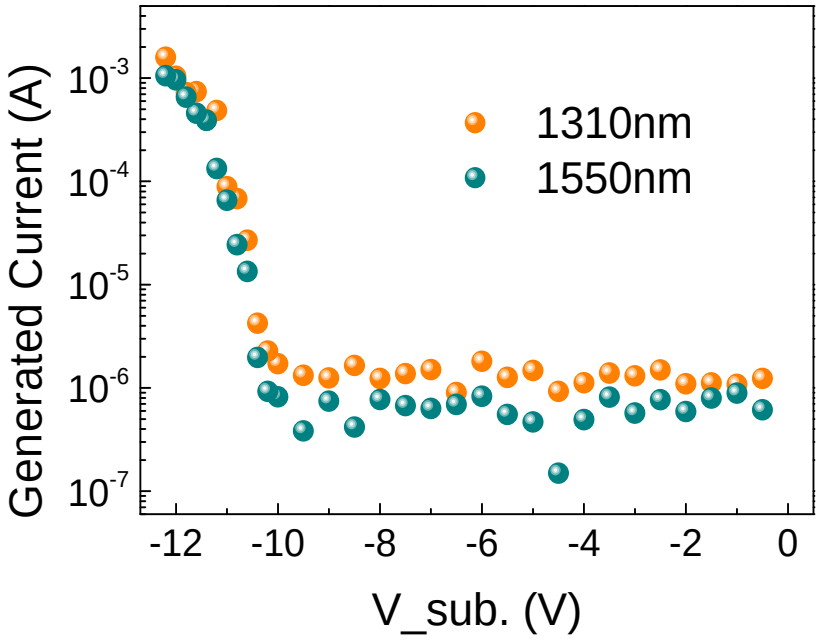

Fig. 5.14 Photo generated current vs. the pulsed substrate bias is plotted under the IR lasers of 1310nm and 1550nm.

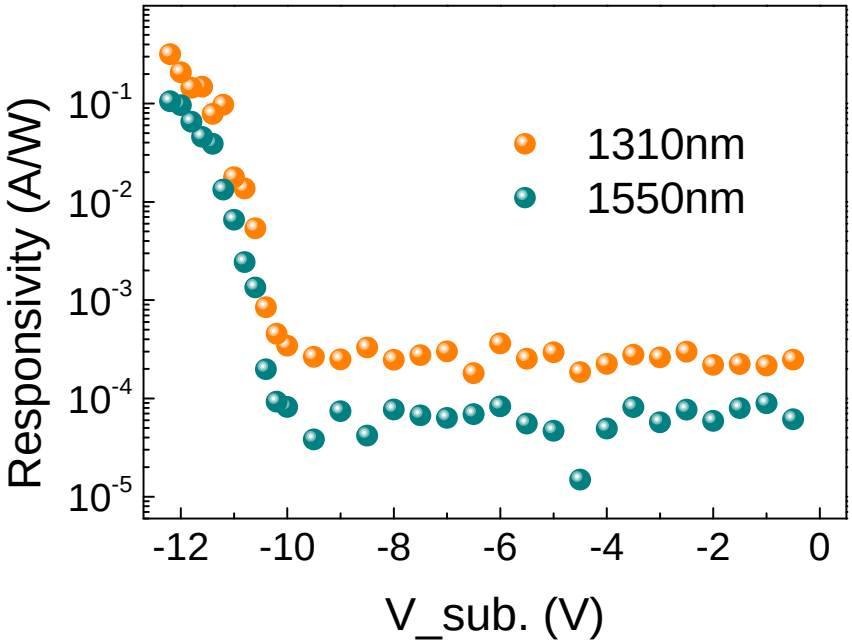

Fig. 5.15 Responsivity vs. the pulsed substrate bias is plotted under the IR lasers of 1310nm and 1550nm.

5.5 Simulated results for the NMOS

For investigating the effect of the lateral electric field with the substrate bias, a numerical simulation for the surface junction of NMOS was conducted. The simulated structure of the NMOS is closely similar to the real integrated device. By way of a brief description of the simulated NMOS structure, the 180nm long gate is N+ polysilicon (1.5×10^{20} cm^{-3}), and the doping concentrations of the P− substrate and the source/drain are 7.78×10^{17} cm^{-3} and 1.1×10^{20} cm^{-3}, respectively. The gate spacer is made of 50nm thick Si_3N_4 and the gate oxide is 3.9 nm thick. For the simulation of the GIDL current of NMOS, Sentaurus with a dynamic non-local path model is used for the band-to-band tunneling (BTBT) in two dimensions [46].

First, for the simulated result, the main mechanism of the GIDL current flow is the BTBT generation at the surface junction. Hence, it is necessary to confirm the region where the electron BTBT is generated. Fig. 5.16 shows the main region of electron generation obtained by the BTBT, which is located at the surface junction. The GIDL current flows from the common source and drain junctions to the Si body. Accordingly, the bias condition for GIDL current is the same bias of 2 V that is applied to the paired source and drain, and is −3 V of the gate. According to the substrate bias of 0 V or −12.0 V, the plot of electric field is distinguished by the difference shown in Fig. 5.17. Even though the substrate bias is applied up to −12 V, the vertical electric field at the depth of 3 nm from the surface exhibits a similar value to that in the case of the 0V substrate bias. However, the lateral electric field shows a large difference in value (approx. 0.5 MV/cm) between the substrate bias of 0 V and −12.0 V. This lateral electric field causes the lateral tunneling current and the multiplication of

GIDL current.

Incidentally, considering the value of the electric field, the value exhibits a range from 0.5–2 MV/cm, which causes an increase in the absorption coefficient for the 1310nm and 1550nm infrareds. From the electric field value, the increase in the absorption coefficient can be calculated as shown in Fig. 5.18. Although the absorption coefficient is extremely small under no electric field, the absorption coefficient increases up to 2.5×10^2/cm and 10/cm for 1310nm and 1550nm infrareds, respectively, when a strong electric field of 1 MV/cm is applied to the surface junction as shown in Fig. 5.18(a). As compared these results with the reference plot data under no electric field, the increased absorption coefficient for 1310nm and 1550nm infrareds exhibits a similar value to that of the 808nm IR in Fig. 5.18(b). This means that the 1310nm and 1550nm infrareds can be absorbed in silicon devices as much as the 808nm IR which has a higher energy than the silicon band-gap energy of 1.12 eV.

This result of increased absorption coefficient for the 1310nm and 1550nm infrareds supports the FKE under the strong electric field bias in the NMOS GIDL surface junction.

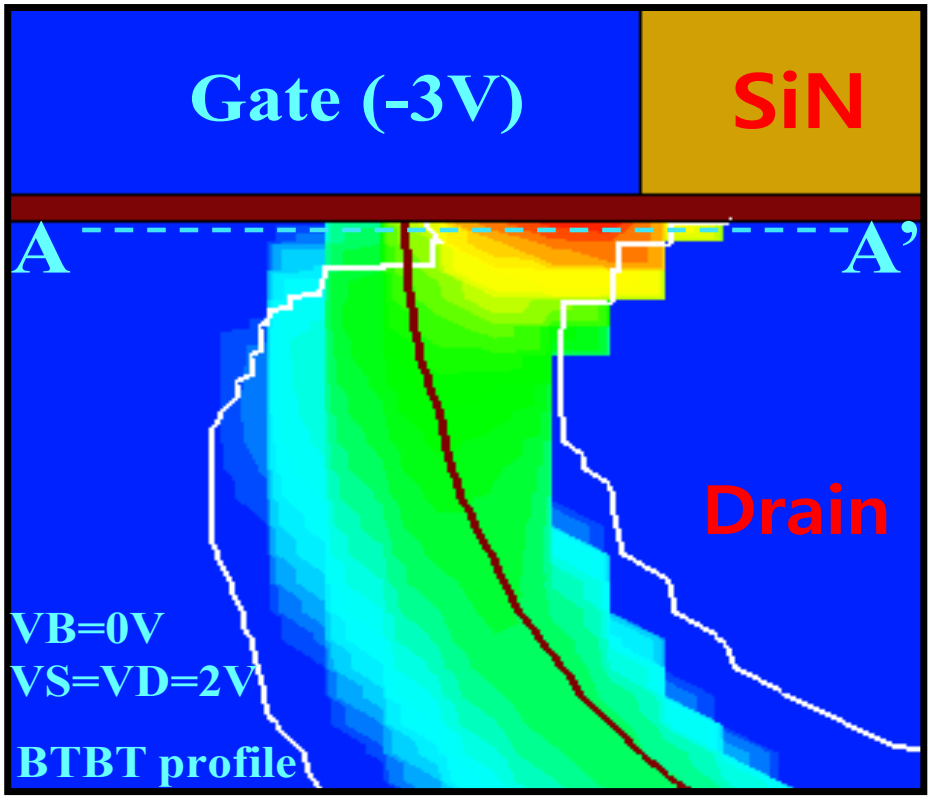

Fig. 5.16 Band to band tunneling profile under the NMOS GIDL bias condition

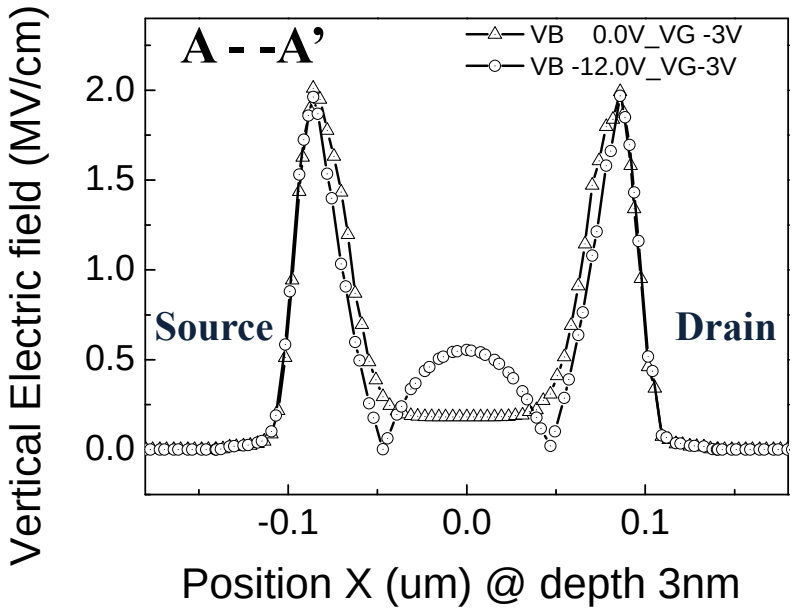

(a)

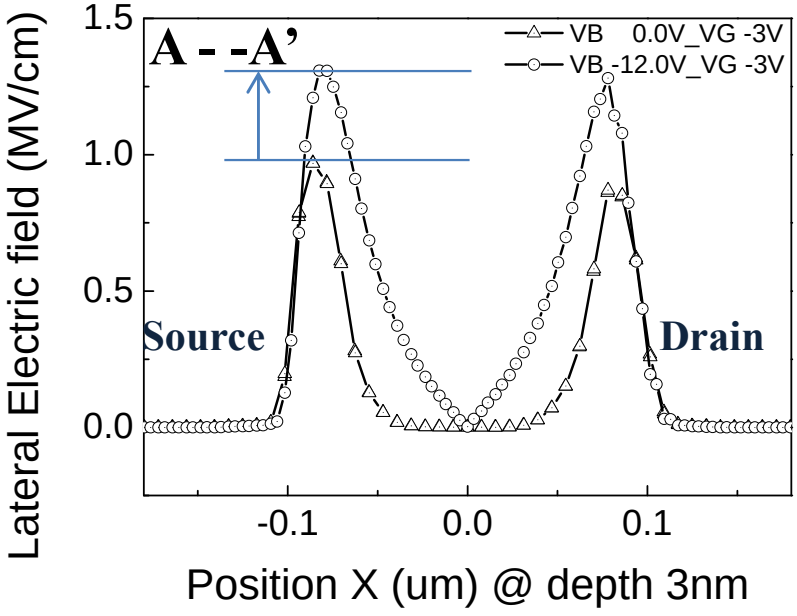

(b)

Fig. 5.17 (a) Vertical electric field and (b) lateral electric filed plot along sliced A—A' at the depth of 3nm from the interface with the gate dielectric.

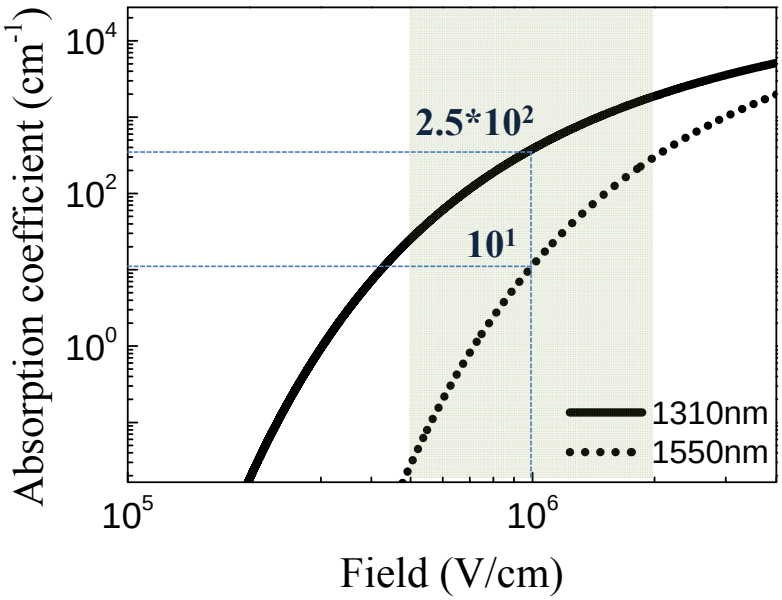

(a)

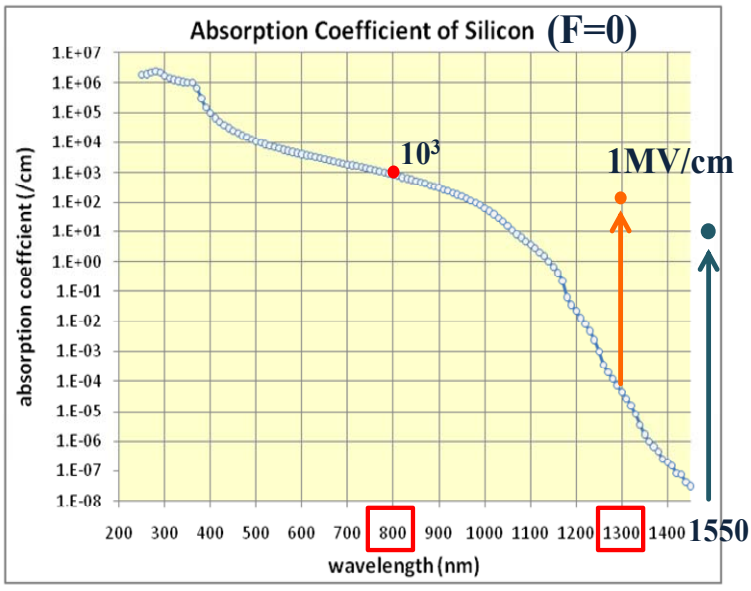

(b)

Fig. 5.18 (a) Absorption coefficient vs. electric field plot for the 1310nm and 1550nm of infrareds, (b) comparison with absorption coefficient under no electric field

Chapter 6

Conclusions

6.1 Summary

In this study, we report the potential to detect the near- infrared light using the conventional Si based Zener diode and the drain and the source surface junction of NMOSFET. The pulsed bias scheme is used to mitigate the negative effect in the responsivity caused by the increase of the junction temperature. With the proper choice of the pulsed bias voltage for the Zener diode, the photo generated signal is amplified by the impact ionization followed by the FKE photo generation and the responsivity of as much as 1.18A/W and 0.89 A/W obtained for NIR at wavelengths of 1310nm and 1550nm, respectively. For the case of MOSFET, the FKE generation is obtained in the surface junction of a MOSFET (called the GIDL region), which gives relatively small responsivity; 0.0362 and 0.0178A/W as compared with the Zener detector for the same NIR wavelengths. However, when the pulsed bias is additionally applied to the substrate, the impact ionization helps for the responsivity to increase up to 0.318 and 0.105A/W for NIR at wavelengths of 1310nm and 1550nm, respectively. The summary of the

experimental results is shown in Table 6.1 in terms of the responsivities whose values are comparable with the result of the normal Ge PDs [8], [10]. Hence, we can conclude that the Si based junctions can be used to detect NIR signal using the FKE generation followed by the multiplication effects by implementing the newly proposed pulse measurement method, which both minimizes the thermal effect and device degradation.

Responsivity (A/W)	**808nm**	**1310nm**	**1550nm**	**Mechanism**
Zener Pulsed Bias	2.27	1.18	0.89	FKE + Multipli.
NMOS Pulse Vb 0.0V	0.484	0.0362	0.0178	FKE
NMOS Pulse Vb12.2V	-	0.318	0.105	FKE + Multipli.
Ge PD [8]	-	-	0.75	p-i-n normal incidence
Ge PD [10]	-	-	1.1	p-i-n waveguide coupled

Table 6.1 Responsivities for experimental devices with the photo current mechanism

6.2 Further works

This dissertation has the result that the detection for the infrared wavelength of 1310nm and 1550nm is possible for Si based devices using the Franz-Keldysh effect. This investigation has been focused on the infrared source with the wavelength of 1310nm and 1550nm, which have an important role at the position in the continental communication. However, it may be necessary to investigate the possibility of detecting longer wavelength of infrareds than 1550nm using the Si based devices such as the Zener diode and the MOSFET.

Finally, the results have been obtained the conventional planar structured NMOS, where the FKE generation region is confined to very shallow surface junction regions. The FKE region may be increased by adopting the 3-dimensional MOSFET structure such as a Si nanowire [69]-[71] or hemispherical surface junction with a bottom gate structure [72]-[73]. If the Si based 3-dimensinal devices are implemented for the infrared detection, the method of the measurement in this dissertation can present to detect the infrared of longer wavelength which is called further work.

References

[1] Antoni Rogalski, “Infrared detectors: status and trends”, OPTOELECTRONICS REVIEW, 1997.

[2] Antoni Rogalski , “Infrared detectors: an overview”, Infrared Physics & Technology 43 (2002) 187–210

[3] C. Y. Chen1, Y. M. Pang1, P. A. Garbinski1, A. Y. Cho1 and K. Alavi1 “Modulation□doped Ga0.47In0.53As/Al0.48In0.52As planar photoconductive detectors for 1.0–1.55□μm applications”, Applied Physics Letters, vol. 43, pp. 308-310, 1983

[4] Campbell, J.C., Tsang, W.T. ; Qua, G.J. ; Johnson, B.C., “High-speed InP/InGaAsP/InGaAs avalanche photodiodes grown by chemical beam epitaxy” IEEE Journal of Quantum Electronics, vol. 24, pp. 496-500, 1988

[5] Shiang-Feng Tang, Shih-Yen Lin, and Si-Chen Lee, “Near-room-temperature operation of an InAs/GaAs quantum-dot infrared photodetector”, APPLIED PHYSICS LETTERS, vol 78, number 17, 23 APRIL 2001.

[6] Rogalski A. and Ciupa R., “Long□wavelength HgCdTe photodiodes: n +□on□p versus p□on□n structures” J. Appl. Phys., vol. 77, pp. 3505-3512, 1995

[7] Sclar, N, “Properties of doped silicon and Germanium infrared detectors”, Prog. Quant. Electr., vol. 9, pp. 149-257, 1984

[8] Silvia Fama`, Lorenzo Colace, Gianlorenzo Masini, and Gaetano Assanto, Hsin-Chiao Luan, “High performance germanium-on-silicon detectors for optical communications” Applied Physics Letters, vol. 81, pp. 586-588, 2002

[9] Jurgen Michel, Jifeng Liu and Lionel C. Kimerling, “High-performance Ge-on-Si photodetectors”, NATURE PHOTONICS | VOL 4 | AUGUST 2010

[10] Dazeng Feng, Shirong Liao, Po Dong, Ning-Ning Feng, Hong Liang, Dawei Zheng, Cheng-Chih Kung, Joan Fong, Roshanak Shafiiha, Jack Cunningham, Ashok V. Krishnamoorthy, and Mehdi Asghari, “High-speed Ge photodetector monolithically integrated with large cross-section silicon-on-insulator waveguide.” Appl. Phys. Lett. 95, 261105 (2009)

[11] Lorenzo Colace, Gianlorenzo Masini, and Gaetano Assanto, “Ge-on-Si Approaches to the Detection of Near-Infrared Light”, IEEE JOURNAL OF QUANTUM ELECTRONICS, vol. 35, no. 12, December 1999.

[12] Shiyang Zhu M. B. Yu, G. Q. Lo, and D. L. Kwong, “Near-infrared waveguide-based nickel silicide Schottky-barrier photodetector for optical communications”, APPLIED PHYSICS LETTERS 92, 081103, 2008

[13] Martin A. Green andMark J. Keever, “Optical properties of intrinsic silicon at 300 K”, Progress in Photovoltaics: Research and Applications. 1995 ;3:189 – 192

[14] M. Rubin., “Optical properties of soda lime silica glasses”, Solar Energy Materials 12, 275-288 (1985).

[15] I. H. Malitson et. al., “Interspecimen Comparison of the Refractive Index of Fused Silica” J. Opt. Soc. Am. 55, 1205-1208 1965

[16] H. R. Philipp., “Optical Properties of Silicon Nitride”, J. Electrochem. Soc. 120, 295-300 (1973)

[17] W. A. CABANSKI and M. J. SCHULZ, “ELECTRONIC AND IR-OPTICAL PROPERTIES OF SILICIDE/SILICON INTERFACES”, Infrared Phys., Vol. 32, pp 29-44, 1991

[18] L. V. Keldysh, “The effect of a strong electric field on the optical properties of insulating crystals,” Sov Phys - JETP, vol. 7, pp. 788–790, 1958.

[19] H. Shen and Fred H. Pollak, “Generalized Franz-Keldysh theory of electro modulation”, Phys. Rev. B 42, pp 7097, 1990

[20] Hernando Garcia, “Tunneling assisted two-photon absorption: The nonlinear Franz-Keldysh effect”, Phys. Rev. B 74, 035212, 2006

[21] Hernando Garcia and Ramki Kalyanaraman, “Phonon-assisted two-photon absorption in the presence of a dc-field: the nonlinear Franz–Keldysh effect in indirect gap semiconductors”, J. Phys. B: At. Mol. Opt. Phys. 39 (2006) 2737–2746

[22] K. THARMALINGAM, “Optical absorption in the presence of a uniform field”, PHYSICAL REVIEW, VOL. 130, NUM. 6, JUNE, 1963

[23] J. Callaway, “Optical absorption in an electric field,” Phys. Rev., vol. 134, pp. A998–A1000, 1964.

[24] L. D. Landau and E. M. Lifshitz, Quantum Mechanics, Addison-Wesley, reading, Mass., 1958, pp 174

[25] Margaret H. Weiler, WIODZIMIERZ ZANADZKI, AND BENJAMIN LAX, “Theory of Tunneling, Including Photon-Assisted Tunneling, in Semiconductors in Crossed and Parallel Electric and Magnetic Fields”, Phys. Rev., vol. 163, pp. 733–742, 1967.

[26] Yuchun Zhou, Yu-hsin Liu, James Cheng, and Yu-Hwa Lo, “Bias Dependence of Sub-Bandgap Light Detection for Core-Shell Silicon Nanowire”, Nano Lett., 12 (11), pp 5929–5935, 2012.

[27] Kotaro Takeda, Tatsuro Hiraki, Tai Tsuchizawa, Hidetaka Nishi, Rai Kou, Hiroshi Fukuda, Tsuyoshi Yamamoto, Yasuhiko Ishikawa, Kazumi Wada, and Koji Yamada, “Contributions of Franz–Keldysh and Avalanche Effects to Responsivity of a Germanium Waveguide Photodiode in the L-Band”, IEEE JOURNAL OF SELECTED TOPICS IN QUANTUM ELECTRONICS, vol. 20, no. 4, July/August 2014.

[28] Tsung-Yang Liow, Andy Eu-Jin Lim, Ning Duan, Mingbin Yu and Guo-Qiang Lo, “Waveguide Germanium Photodetector with High Bandwidth and High L-band Responsivity”, Optical Fiber Communication Conference, Anaheim, California United States, March 17-21, 2013.

[29] RICHARD B. FAIR, HAYDEN W. WIVELL, “Zener and Avalanche Breakdown in As-Implanted Low-Voltage Si n-p Junctions”, IEEE, Transaction on Electron Devices, Vol. 23, No. 5, May, 1976.

[30] G.A.M. Hurks, H. C. de Graaff, W. J. Kloosterman, and M. P. G.

Knuvers, “A New Analytical Diode Model Including and Avalanche Breakdown”, IEEE, TRANSACTIONS ON ELECTRON DEVICES, vol. 39, issue 9, pp 2090-2098.

[31] CLARENCE ZENER, H. H. Wills Physics Laboratory, Bristol, “A Theory of the Electrical Breakdown of Solid Dielectrics”, Proceedings of the Royal Society of London. Series A, Containing Papers of a Mathematical and Physical Character, Vol. 145, No. 855 (Jul. 2, 1934), pp. 523-529

[32] M. SINGH TYAGI, “ZENER AND AVALANCHE BREAKDOWN IN SILICON ALLOYED p-n JUNCTIONS”, Solid-State Electronics, Vol. 11, pp. 99-115, 1968.

[33] C. R. Crowell and S. M. Sze, “TEMPERATURE DEPENDENCE OF AVALANCHE MULTIPLICATION IN SEMICONDUCTORS”, Appl. Phys. Lett. 9, 242 (1966)

[34] M. Sparks, D. L. Mills, R. Warren, T. Holstein, A. A. Maradudin, L. J. Sham, E. Loh. Jr., and D. F. King, “Theory of electron-avalanche breakdown in solids”, PHYSICAL REVIEW B VOLUME 24, NUMBER 6, SEPTEMBER 1981

[35] Henrike Trompeter, Thomas Pertsch, Falk Lederer, Dirk Michaelis, Ulrich Streppel, Andreas Bra¨uer, and Ulf Peschel, “Visual Observation of Zener Tunneling”, PHYSICAL REVIEW LETTERS, 96, 023901 (2006).

[36] Jyh-Chyurn Guo, Yuan-Chang Liu, M. H. Chou, M. T. Wang, and F.

Shone, “A three-terminal band-trap-band tunneling model for drain engineering and substrate bias effect on GIDL in MOSFET” , IEEE Transaction on Electron Devices vol. 45, issue 7, pp 1518-1523

[37] Kaushick Roy, S Mukhopadhyay “Leakage Current Mechanisms and Leakage Reduction Techniques in Deep-Submicrometer CMOS Circuits”, PROCEEDINGS OF THE IEEE, vol. 91, no. 2, FEB. 2003.

[38] MARIOUS ORLOWSKI, SHIH WEI SUN, PETER BLAKEY, and RAVI SUBRAHMANYAN, “The combined effects of band-to-band tunneling and impact ionization in the off regime of an LDD MOSFET”, IEEE, EDL, VOL. 11, NO. 12, DECEMBER 1990.

[39] Y. Omrot and C. R. CROWEL, “Threshold energy effect on avalanche breakdown voltage in semiconductor junctions”, Solid-State Electronics, 1975, Vol. 18, pp. 16146.

[40] C. L. Forrest Ma, M. Jamal Deen, Senior Member, Larry E. Tarof, and Jeffrey C. H.Yu “Temperature Dependence of Breakdown Voltages in Separate Absorption, Grading, Charge, and Multiplication InP/InGaAs Avalanche Photodiodes”, IEEE TRANSACTIONS ON ELECTRON DEVICES, VOL. 42, NO. 5, MAY 1995

[41] P.H. Wendland and Marvin Chester, “Electric Field Effects on Indirect Optical Transitions in Silicon”, Phys. Rev., vol. 140, Num. 15 November 1965.

[42] William Vandenberghe, Bart Sor´ee, Wim Magnus, Massimo, and V. Fischetti, “Generalized phonon-assisted Zener tunneling in indirect

semiconductors with non-uniform electric fields : a rigorous approach", JOURNAL OF APPLIED PHYSICS 109, 124503 (2011)

[43] V. Golovin, V. Save-liev, "Novel type of avalanche photodetector with Geiger mode operation", Nuclear Instruments and Methods in Physics Research Section A: Accelerators, Spectrometers, Detectors and Associated Equipment, vol. 518, issues 1-2, pp 560-564, Feb., 2004.

[44] K. G. McKwv, "Avalanche Breakdown in Silicon", PHYSICAL REVI EW VOLUM E 94, NUM HER 4 MAY 15, 1954

[45] D. Renker, "Geiger-mode avalanche photodiodes, history, properties and problems", Nuclear Instruments and Methods in Physics Research Section A: Accelerators, Spectrometers, Detectors and Associated Equipment, vol. 567, issues 1, pp 48-56, Nov., 2006.

[46] E. O. kane, "Theory of tunneling", Journal of Appl. Phys., 32, 83, 1961.

[47] Markus Rosar, Bernard Leroy, and Giorgio Schweeger, "A new model for the description of gate voltage and temperature dependence of gate induced drain leakage (GIDL) in the low electric field region [DRAMs]", IEEE TRANSACTIONS ON ELECTRON DEVICES, VOL. 47, NO. 1, JANUARY 2000.

[48] K. Saino, S. Horiba, S. Uchiyama, Y. Takaishi, M. Takenaka, T. Uchida, Y. Takada, K. Koyama, H. Miyake, and C. Hu, "Impact of Gate-Induced Drain Leakage Current on the Tail Distribution of DRAM Data Retention Time", Electron Devices Meeting, 2000, IEDM.

[49] K. Rais. F. Balestra and G Ghibaudo, "Temperature dependence of gate

induced drain leakage current in silicon CMOS devices", ELECTRONICS LETTERS 6th January 1994 Vol. 30 No. 1

[50] V. Nathan and N. C. Das, "Gate-Induced Drain Leakage Current in MOS Devices", IEEE TRANSACTIONS ON ELECTRON DEVICES, VOL. 40, NO. 10, OCTOBER 1993.

[51] Sung-il CHANG, Jongho LEE and Hyungcheol SHIN, "Gate-Induced Drain Leakage Currents in Metal Oxide Semiconductor Field Effect Transistors with High-κ Dielectric", Jpn. J. Appl. Phys. Vol. 41 (2002) pp. 4432–4435

[52] Oleg semenov, Andrzej Pradzynski, Manoj Sachdev, "Impact of gate induced drain leakage on overall leakage of submicrometer CMOS VLSI circuits", IEEE transactions on semiconductor manufacturing, vol 11, 2002, SS:11-15.

[53] J. Chen, T. Y. CHAN, J. C. CHEN, P. K. KO, and CHENMING HU, "Subbreakdown drain leakage current in MOSFET", IEEE, EDL, VOL. EDL-8, NO. 11, NOVEMBER 1987.

[54] Ming-Jer Chen, Member, Huan-Tsung Huang, Chin-Shan Hou, and Kuo-Nan Yang, "Back-Gate Bias Enhanced Band-to-Band Tunneling Leakage in Scaled MOSFET's", IEEE ELECTRON DEVICE LETTERS, VOL. 19, NO. 4, APRIL 1998.

[55] L. Huang, P.T. Lai, J.P. Xu, Y.C. Cheng, "Mechanism analysis of gate-induced drain leakage in off-state n-MOSFET", Microelectronics Reliability 38 (1998) 1425-1431.

[56] SHUN LIEN CHUANG, “PHYSICS OF PHOTONIC DEVICES”, WILEY, second edition, 2009

[57] N. Azizi, Peter Yiannacouras, “Gate Oxide Breakdown”, Lecture Notes, Reliability of Integrated Circuits, 2003.

[58] JACK C. Lee, IH-CHIN CHEN, and CHENMING HU, “Modeling and Characterization of Gate Oxide Reliability”, IEEE TRANSACTIONS ON ELECTRON DEVICES, VOL. 35. NO. 12, DEC., 1988.

[59] Cheung, K. P., “A physics-based, unified gate-oxide breakdown mode”, International Electron Devices Meeting, pp 719-722, 5-8 Dec., 1999.

[60] Chen Haifeng, Du Huimin, Guo Lixin, “Effect of Substrate Negative Bias on GIDL Current in LDD nMOSFET's”, 2011 International Conference on Mechatronic Science, Electric Engineering and Computer August 19-22, 2011

[61] T.Endoh, R.Shirota, M. Momodomi, and F.Masuoka, “An accurate model of subbreakdown due to band-to-band tunneling and some applications”, IEEE Trans. Electron Device, YRO 37, 1990, SS:290- 295

[62] R. Shirota, T. Endoh, M. Momodomi, R. Nakayama, S. Inoue, R. Kirisawa, and F. Masuoka, “An accurate model of subbreakdown due to band to-band tunneling and its application,” in IEDM Tech. Dig., 1988, pp. 26-29

[63] Kosonocky, Walter F., Shallcross, F.V. ; Villani, T.S., “160 × 244 Element PtSi Schottky-barrier IR-CCD image sensor”, IEEE, Transaction on Electron Devices, Vol. 32, Issue 8, 2005

[64] W.A. Cabanski, M.J. Schulz, “Electronic and IR-optical properties of silicide/silicon interfaces”, Infrared Physics, Vol. 32, pp 29-44, 1991

[65] Shiyang Zhu, M. B. Yu, G. Q. Lo, and D. L. Kwong, “Near-infrared waveguide-based nickel silicide Schottky-barrier photodetector for optical communications”, Appl. Phys. Lett. 92, 081103, 2008

[66] Ming-Kwei Lee, Chi-Hsing Chu, and Yu-Hsiung Wang, “1.55-mm and infrared-band photoresponsivity of a Schottky barrier porous silicon photodetector”, OPTICS LETTERS / Vol. 26, No. 3 / February 1, 2001

[67] Christine Scales, and Pierre Berini, “Thin-Film Schottky Barrier Photodetector Models”, IEEE JOURNAL OF QUANTUM ELECTRONICS VOL. 46, NO. 5, MAY 2010

[68] Ja-Hao Chen, Shyh-Chyi Wong, and Yeong-Her Wang, “An Analytic Three-Terminal Band-to-Band Tunneling Model on GIDL in MOSFET”, IEEE TRANSACTIONS ON ELECTRON DEVICES, VOL. 48, NO. 7, JULY 2001

[69] L. Tsakalakos, J. Balch, J. Fronheiser, and B. A. Korevaar, “Silicon nanowire solar cells”, Appl. Phys. Lett. 91, 233117 (2007).

[70] Yu Yun Seop Yu1, Se Han Lee, Jung Hyun Oh, Han Jung Kim1, Sung Woo Hwang and Doyel Ahn, “A compact analytical current conduction model for a depletion-mode n-type nanowire field-effect transistor with a bottom-gate structure”, Semicond. Sci. Technol. 23 035025 2008.

[71] Erik Garnett and Peidong Yang, “Light Trapping in Silicon Nanowire Solar Cells”, Nano Lett., 2010, 10(3), pp 1082-1087.

[72] Jia Zhu Jia Zhu, Ching-Mei Hsu, Zongfu Yu, Shanhui Fan, and Yi Cui, “Nanodome Solar Cells with Efficient Light Management and Self-Cleaning”, Nano Lett., 2010, 10, pp 1979-1984.

[73] C. S. Yang, W. W. Read, C. Arthur, E. Srinivasan, and G. N. Parsons, “Self-Aligned Gate and Source Drain Contacts in Inverted-Staggered a-Si:H Thin-Film Transistors Fabricated Using Selective Area Silicon PECVD”, IEEE ELECTRON DEVICE LETTERS, VOL. 19, NO. 6, JUNE 1998.

초 록

근적외선은 780nm ~ 2500nm 영역의 파장을 가지며 에너지는 0.48eV~1.58eV를 갖는다. 일반적으로 근적외선을 흡수하는 장치로 적용되는 물질은 인듐갈륨아세나이드, 게르마늄, 피비실리사이드 등이 있는데 이는 실제 제작 하는 데에 있어 경제적 비용이 많이 들고 전기적 반도체 장치로서 널리 이용되고 있는 실리콘 제작 공정과 호환하기 어려운 문제점이 있다.

이러한 관점에서 본 논문은 실리콘 공정만으로 만들어진 소자를 이용하여 근적외선을 탐지하는 시도를 하고자 하는데 있다. 실리콘을 적외선 탐지하는 장치로 적용하려 할 때에 가장 큰 걸림돌은 실리콘의 밴드갭 에너지가 1.12eV로서 1150nm 이상의 파장을 가지는 적외선에 대해서는 흡수가 일어나지 않는 데에 있다. 이를 가능케 하는 이론으로 프란츠-켈디쉬 효과가 있다. 프란츠-켈디쉬 효과는 통상 조건에서는 실리콘의 밴드갭 에너지보다 작은 에너지의 빛을 흡수하지 못하지만 강한 전계가 인가되어 터널링 전류의 흐름이 있는 조건에서는 흡수가 발생할 수 있다는 이론이다.

이를 검증하기 위해 본 논문에서는 터널링 전류가 발생할 수 있는 실리콘 반도체 장치로서 제너 다이오드와 모스펫을 이용하려 한다. 제너 다이오드의 경우 강한 반대방향 전계가 인가 될 경우 터널링 전류가 발생하며, 모스펫의 경우 게이트 와 드레인사이에 강한 전계가 인가되는 조건의 경우 역시 터널링 전류가 발생하게 된다. 이러한 전계 조건에서 실리콘의 밴드갭 에너지보다 작은 에너지를 갖는

1310nm 와 1550nm 의 파장의 적외선을 조사하여 흡수가 일어날 수 있게 하였다. 또한 더 많은 흡수를 발생시키기 위해 제너 다이오드의 경우 터널링 전류가 흐르는 전계 조건 보다 더 강한 전계를 인가하여 애벌런치 멀티플리케이션을 발생시켰다. 그런데 애벌런치 멀티플리케이션이 발생하는 전계 영역에서는 정션의 줄 열 발생에 의한 음의 온도계수가 존재하므로 이를 억제하기 위해 펄스 전계 인가 기법을 적용하였고 터널링 전류만 발생하는 전계 영역에서보다 더 많은 광 전류를 도출 할 수 있었다. 모스펫의 경우에도 게이트 와 드레인사이에 강한 전계가 인가되는 조건에서 역시 실리콘의 밴드갭 에너지보다 작은 에너지를 갖는 1310nm 와 1550nm 의 파장의 적외선을 조사하여 흡수가 일어날 수 있게 하였고 더 많은 흡수를 위해 실리콘 기판의 전계를 음수로 강하게 인가하여 광 전류의 멀티플리케이션을 일으켜 확대된 적외선 신호를 얻을 수 있었다. 결론적으로 이 연구를 통하여 두 가지의 실리콘 디바이스를 이용하여 적외선 신호에 반응하는 탐지기로서의 기능을 확인 하였고 제너 다이오드와 모스펫으로 적외선을 탐지할 수 있는 장치로 이용 가능하다는 것을 확인하였다.

주요어: 프란츠 켈디쉬 효과, 근적외선, 제너 다이오드, 펄스 측정, 모스펫 기들 전류, 터널링 전류, 애벌런치 멀티플리케이션, 포지티브 템퍼러쳐 코이피션트, 네가티브 템퍼러쳐 코이피션트, 응답성.